FACULDADE DE ENGENHARIA DA UNIVERSIDADE DO PORTO

Electrical Boosting: Assessment of the Electric Energy Transfer in Glass Furnaces

Pedro Luiz Dias Barroso



Master in Environmental Engineering

Supervisor: Dr. José Carlos Magalhães Pires

Company Supervisor: Dr. Paulo Jorge da Cunha Gomes

President of the Jury: Dr. Adrián Manuel Tavares da Silva

Member of the Jury: Dr. Mariana Garcia Domingos

July 31, 2023

Resumo

Na indústria vidreira, o método de operação predominante dos fornos de fabrico de vidro baseia-se na combustão de gás natural. No entanto, devido às preocupações com as alterações climáticas e à volatilidade dos preços do gás natural observada em 2022, criou-se um interesse crescente em opções alternativas, mais fiáveis e ecológicas. O *boosting* elétrico surgiu como uma solução viável, uma vez que depende exclusivamente da eletricidade e pode complementar a energia utilizada na produção de vidro com os métodos de combustão tradicionais. Para avaliar a eficiência deste equipamento, que converte energia eléctrica em energia térmica através do efeito Joule, foi desenvolvido um modelo matemático detalhado.

Este modelo matemático foi construído com base na configuração de um forno representativo e nos principais dados operacionais, incluindo a voltagem e a corrente elétrica aplicada, e a composição química da mistura de vidro fundido. Foi utilizada uma abordagem aritmética, sem considerar as desfasagens entre fases. O modelo avaliou a eficiência de cada fase individualmente, assim como a eficiência global do sistema. Também estimou a dissipação de energia, o volume de influência e a sua respectiva taxa de aumento de temperatura para cada elétrodo do sistema.

Em vários cenários, a eficiência das fases individuais variou entre 57 % e 96 %, enquanto que, considerando todas as fases em conjunto, a eficiência global variou entre 63 % e 69 %. Uma análise de sensibilidade aos dados também foi realizada. Observou-se que 10 dos 12 eléctrodos tiveram uma influência significativa em toda a fusão do vidro, enquanto os dois restantes tiveram um impacto mais localizado. De acordo com as expectativas, observou-se que a taxa de aumento da temperatura nos eléctrodos que exerceram uma influência significativa num volume maior do vidro fundido foi comparativamente mais baixa. Em contrapartida, os eléctrodos que influenciaram volumes menores apresentaram taxas de aumento de temperatura aproximadamente 100 vezes superiores.

Além disso, uma avaliação da densidade de corrente na superfície dos eléctrodos revelou um resultado preocupante. Em todos os cenários, os eléctrodos da fase terciária apresentaram consistentemente valores de densidade de corrente que excederam o limite máximo de segurança. Este resultado suscita preocupações significativas relativamente ao potencial de desgaste acelerado e degradação destes eléctrodos. O desenvolvimento do modelo matemático revelou uma falta significativa de informação disponível sobre a construção e a otimização de sistemas de *boosting* elétrico.

Palavras-chave: *Boosting* elétrico; Resistividade eléctrica; Dissipação de potência; Fornos de fabrico de vidro; Produção de vidro.

Abstract

In the glass industry, the predominant method for glass furnace operation relies on natural gas combustion. However, due to concerns about climate change and the volatility of natural gas prices observed in 2022, there is growing interest in alternative, more reliable, and environmentally friendly options. Electrical boosting has emerged as a viable solution, as it exclusively relies on electricity and can supplement the energy input in glass production alongside traditional combustion methods. To assess the efficiency of this system, which converts electrical energy into thermal energy through the Joule effect, a comprehensive mathematical model was developed.

The mathematical model was constructed based on a representative furnace layout and key operational data, including voltage, current, and chemical composition of the melted glass mixture. An arithmetical approach was adopted, without considering phase mismatches. The model evaluated the efficiency of each phase individually, as well as the overall system efficiency. It also estimated the power dissipation, influence volume, and temperature increase rate for each electrode within the system.

Across various scenarios, the efficiency of individual phases ranged from 57 % to 96 %, while considering all phases together, the overall efficiency ranged from 63 % to 69 %. A sensitivity analysis was also performed on the data. It was observed that 10 out of the 12 electrodes had a significant influence on the entire glass melt, while the remaining two had a more localised impact. Consistent with expectations, it was observed that the temperature increase rate in electrodes that exerted a significant influence on a larger volume of the glass melt was comparatively lower. In contrast, electrodes that influenced smaller volumes exhibited temperature increase rates that were approximately 100 times higher.

Additionally, an evaluation of the current density on the surface of the electrodes revealed a concerning result. In all scenarios, the electrodes from the tertiary phase consistently exhibited current density values that exceeded the maximum safe limit. This finding raises significant concerns regarding the potential for accelerated wear and degradation of these electrodes. The process of developing the mathematical model revealed a significant lack of available information regarding the design and optimisation of electrical boosting systems.

Keywords: Electrical boosting; Electrical resistivity; Power dissipation; Glass furnaces; Glass production.

Acknowledgements

First and foremost, I would like to express my heartfelt gratitude to my supervisors, Dr. Paulo Jorge da Cunha Santos and Prof. Dr. José Carlos Pires Magalhães, for generously sharing their knowledge, providing guidance throughout this work, and being readily available for consultations.

I would also like to extend my appreciation to the Data Science and Analytics team at BA Glass, namely Daniel, Gustavo, José, and Nikkitha, for warmly welcoming me as a valued member of the team and for the unwavering support they have provided.

I am sincerely appreciative of all the employees at BA Glass from various teams who, in different ways, contributed to the development of this work. I would like to express my special thanks to Engineers Horácio, Pedro, and Vitor from the Investments team, as well as Tiago from the Electrical Maintenance team, for their assistance and collaboration.

I want to thank my colleague and friend Raquel, who has been by my side throughout this intense five-year journey at FEUP. Together, we have overcome the most challenging and stressful moments, and our healthy competition has undoubtedly played a role in achieving our high grades.

I am immensely grateful to my friends who have provided unwavering support during this demanding period, even when physical distance separated us. It has become evident along this journey who my true companions are.

I am truly grateful to Sarah, my incredible almost-Brazilian English girlfriend, who has continuously motivated and supported me throughout the challenges during this period despite our long-distance relationship. Your presence in my life has brought a fresh perspective, immeasurable joy, and a renewed appreciation for the world around us. Thank you for embarking on this remarkable journey with me, as we explore the beauty of this small world together.

I want to extend my deepest appreciation to my father, Mauro, and my mother, Lucemar, who, despite being on the other side of the world, entrusted a 17-year-old Pedro to venture alone to another continent. Their constant support has been instrumental in shaping my academic career since my younger years. I also want to acknowledge my sister, Maria, with whom I share my European life, despite the occasional moments of stress. Last but not least, I want to mention my brother, Luiz, his wife, Carol, and their adorable daughters, Laura and Maya, whom I dearly miss.

Lastly, I want to extend sincere appreciation to myself for transforming my dreams into tangible objectives and relentlessly pursuing them. It took immense courage to let go of my old lifestyle, consistently push beyond my comfort zone, and embrace new opportunities that life has to offer. I want to acknowledge and thank myself for remaining authentic and true, unwavering in my commitment to being the best version of me.

The wave pool dream from the young Bombinhas kid is still alive.

Pedro Barroso

Funding

Dr. José Carlos Magalhães Pires, supervisor of this dissertation is an integrated member of LEPABE – Laboratory for Process Engineering, Environment, Biotechnology and Energy, financially supported by LA/P/0045/2020 (ALiCE), UIDB/00511/2020 and UIDP/00511/2020 (LEPABE), funded by national funds through FCT/MCTES (PIDDAC).

"It is necessary to dream, but with the condition of believing in our dreams.
To examine real life carefully, to confront our observation with our dreams,
and to perform our fantasy scrupulously."

Vladimir Ilyich Ulyanov

Contents

Resumo i

Abstract ii

Acknowledgments iii

Funding iv

List of Figures viii

List of Tables ix

Abbreviations x

1 Introduction 1
- 1.1 Motivation . . . 1
- 1.2 Company Description . . . 2
- 1.3 Objectives . . . 3
- 1.4 Thesis Outline . . . 3

2 State-of-the-art 4
- 2.1 Glass-making Industry . . . 4
- 2.2 Glass Composition . . . 8
- 2.3 Electrical Properties . . . 9
  - 2.3.1 Electrical Resistance . . . 10

3 Methodology 12
- 3.1 Furnace Data . . . 12
  - 3.1.1 Furnace Layout . . . 12
  - 3.1.2 Operational Parameters . . . 14
- 3.2 Methods . . . 16
  - 3.2.1 Resistivity Model . . . 17
  - 3.2.2 Resistance Calculation . . . 20
  - 3.2.3 Power Dissipation Calculation . . . 23
  - 3.2.4 Heat Transfer Calculation . . . 24
  - 3.2.5 Sensitivity Analysis . . . 25

4 Results and Discussion **26**
4.1 Electrical Resistivity 26
4.2 Electrical Resistance 28
4.3 Power Dissipation 33
4.4 Heat Transfer 36
4.5 Sensibility Analysis 39

5 Conclusions **41**
5.1 Achievements 41
5.2 Future Work 42

A Model Coefficients **47**

B Dimensional Parameters **49**

C Results Values **51**

List of Figures

2.1 Soda-lime-silica (flat glasses on the left side, container glasses on the right side) and borosilicate glasses (laboratory glassware, in the middle), adapted [11–13]. . 5
2.2 Glass Container Production Process, adapted [15]. 6
2.3 Representation of an end-port fired furnace [17]. 7
2.4 Representation of a sidewall boosting system for an end-port fired furnace, adapted [22]. 10

3.1 Representation of the electrical boosting system in the furnace and its measurements. 13
3.2 Representation of the perfect imaginary cylinder of molten glass, adapted [30]. . 24

4.1 Representation of the logarithmic function of the glass melt electrical resistivity, for Mazurin and Fluegel models, and their extrapolation from 1400 to 1550 ºC. . 27
4.2 Representation of the function of the glass melt electrical resistivity, for Mazurin and Fluegel models, and their extrapolation from 1400 to 1550 ºC. 27
4.3 Dependence of the effective power ($P_{u,\,Ei}$) and square current (I^2_{Ei}) ratio on the imaginary cylinder radius (X). 35

List of Tables

2.1 Typical SLS glass composition range, adapted [18] 8
2.2 Average container glass composition by colour, adapted [19] 8

3.1 Chemical composition of the glass melt for the 4 scenarios 14
3.2 Electrical boosting parameters for 4 different days of production 15
3.3 Electric current on each electrode for 4 different days of production 16
3.4 The applicable compositional range for Mazurin model, adapted [36] 18

4.1 Electrical resistivity values obtained from the two models 28
4.2 Effective power dissipated from each electrode 29
4.3 Calculated operational parameters 30
4.4 Current density on each electrode, disregarding any wear from erosion 32
4.5 Current density on each electrode, considering wear from erosion 32
4.6 Power generated from the electrode resistance 33
4.7 Radius X of the perfect imaginary cylinder around the electrode 34
4.8 The calculated volume of the perfect imaginary cylinder around the electrode . . 37
4.9 Temperature increase rate on the perfect imaginary cylinder around the electrode 37
4.10 Sensibility analysis on operational parameters for scenarios 1 and 2 39
4.11 Sensibility analysis on operational parameters for scenarios 3 and 4 39

A.1 Compositional coefficients for Mazurin electrical resistivity model, adapted [36] . 47
A.2 Compositional coefficients for Fluegel electrical resistivity model, adapted [35] . 48

B.1 Distance between each pair of electrode 49
B.2 Distance between each pair of electrode (cont.) 50

C.1 Effective power dissipated from each electrode pair 51
C.2 Effective power dissipated from each electrode pair (cont.) 52

Nomenclature

Acronyms

AC	Alternating-current
SEC	Specific energy consumption
SLS	Soda-lime-silica
VFT	Vogel-Fulcher-Tamman

Math Operators

$\cdot$	Dot product operator
exp	Natural exponential
ln	Natural logarithm
$\log_{10}$	Base-10 logarithm
$\sum$	Sum of multiple terms
$\int dx$	Integral in order to x

Greek Symbols

β_i	Component i^{th} first-order coefficient
β_{ik}	Component ik^{th} second-order coefficient
β_{ikm}	Component ikm^{th} third-order coefficient
β_o	Model intercept
γ	Glass density (kg m^{-3})
η_{phase}	Efficiency of the conversion of the phase power
η_{RST}	Efficiency of the conversion of the system power
ρ	Glass melt electrical resistivity (Ω m)
ρ_e	Electrode electrical resistivity (Ω m)
ρ_T	Glass melt electrical resistivity at temperature T (Ω m)

Roman Symbols

A	Cross-sectional area (m^2)
B	VFT composition-dependent parameter
B_i	VFT composition-dependent parameter of the i^{th} component
B_{ik}	VFT composition-dependent parameter of the ik^{th} component
B_{ikm}	VFT composition-dependent parameter of the ikm^{th} component
b_{ik}	Distance between electrodes i and k (m)
C	VFT composition-dependent parameter
C_i	VFT composition-dependent parameter of the i^{th} component
c_p	Specific heat of the glass melt at constant pressure $\left(\text{kJ kg}^{-1}\ ^{\circ}\text{C}^{-1}\right)$
d	Diameter of the electrode (m)

Roman Symbols (cont.)

$I_{d,\,E_i}$	Electric current density on the electrode i on its initial measurements ($\mathrm{A}\cdot\mathrm{cm}^{-2}$)
$I_{d-c,\,E_i}$	Electric current density on the electrode i considering operational wear ($\mathrm{A}\cdot\mathrm{cm}^{-2}$)
I_{E_i}	Electric current on the electrode i (A)
I_{phase}	Phase electric current (A)
L	Length of the conductor (m)
l	Length of the electrode (m)
M	Intermediate VFT parameter
m	Mass of the imaginary cylinder around the electrode (kg)
m_i	Mass of the imaginary cylinder around the electrode i (kg)
N	Intermediate VFT parameter
n	Number of significant components
n_e	Number of significant terms for the sum
$P_{R,\,Ei}$	Power generated by the electrode resistance (kW)
$P_{t,\,phase}$	Theoretical power provided by a phase (kW)
$P_{t,\,RST}$	Total effective theoretical provided by the system (kW)
$P_{u,\,Ei}$	Effective power dissipated from electrode i (kW)
$P_{u,\,ik}$	Effective power dissipated by the i and k electrode pair (kW)
$P_{u,\,phase}$	Effective power dissipated by a phase (kW)
$P_{u,\,RST}$	Total effective power inserted in the glass (kW)
R	Electrical resistance (Ω)
R_e	Electrode electrical resistance (Ω)
R_{ik}	Electrical resistance between electrodes i and k (Ω)
T	Temperature ($^\circ$C)
T_f	Final temperature ($^\circ$C)
T_i	Initial temperature ($^\circ$C)
T_0	VFT composition-dependent parameter
$T_{0,\,i}$	VFT composition-dependent parameter of the i^{th} component
t	Time (s)
U_i	Voltage to ground from electrode i (V)
U_k	Voltage to ground from electrode k (V)
U_{phase}	Phase voltage (V)
$U_{terminal}$	Voltage to ground on a terminal (V)
V_{gm}	Total volume of the glass melt (m^3)
V_i	Volume of the perfect imaginary glass cylinder for the i^{th} electrode (m^3)
X	Radius of the perfect imaginary cylinder around the electrode (m)
X_{eq}	Equivalent radius of the perfect imaginary glass cylinder for the total glass melt volume (m)
X_i	Radius of the perfect imaginary cylinder around the electrode i (m)
x_i	Component i^{th} mole percent (mol%)
x_k	Component k^{th} mole percent (mol%)
x_m	Component m^{th} mole percent (mol%)

Chapter 1

Introduction

This thesis is part of the Dissertation course unit of the Master's Program in Environmental Engineering at the Faculty of Engineering, University of Porto. The thesis work had a duration of 5 months, starting in February 2023 and ending in June 2023. The work was developed in the Data Science and Analytics division at the headquarters of BA Glass, located in Vila Nova de Gaia, Portugal.

1.1 Motivation

Natural gas has been a concern for the industries which depend on it. Its price instability observed, mainly in Europe, caused by the Russia-Ukraine War, brought up the economic reliability of its use. Not only for financial, but environmental reasons have come up as a hot topic between governments and companies. Such as any fossil fuel, natural gas combustion generates greenhouse gases, which implies an increase in global warming, and consequently, in climate changes. Meanwhile, electricity and renewable sources earned even more attention as an option to succeed in this situation.

Due to these increases in concerns about climate change, national and international protocols were created to set realistic and achievable goals, such as the climate-neutral by 2050 set by the European Union. For the glass-making industry, the Carbon Neutrality by 2050 plan implies a replacement of the consumption of fossil fuel energy with renewable energy, an increase of the volume of recycled glass by at least 70 % and the capability of producing renewable energy for self-consumption. Another existent is the Porto Protocol, which mainly brings the commitment to using a minimum of 70 % of electricity from renewable sources and reducing natural gas use by 10 %, besides reaching the European Union's carbon dioxide emissions target levels, at least [1].

BA Glass has one of the most modern furnaces in the industry where most studies and upgrades take place. The work carried out in this thesis will use that same furnace as reference, mainly because it is the furnace from where the company has more data. One of the studies done on this furnace, still in development, is a *Furnace Digital Twin*: a furnace simulation algorithm

that will be able to quantify energy requirements in quasi-real time. The *Digital Twin* project aims to simulate all the complexity regarding a glass-melting tank and calculate the minimum energy required to operate the production, considering all the energy inputs (such as combustion and electrical boosting energy), outputs (e.g. wall losses), and energy requirements (e.g. endothermic reactions, latent and sensible heat requirement).

The proposal of this thesis aims at creating a boosting methodology to calculate the electric contributions in the energy balance of the furnace. This model has the potential to be included in the *Digital Twin* mentioned above. A further reduction in energy consumption can happen due to its validation. To the date of this thesis, no similar publications have been found.

1.2 Company Description

BA Glass is a Portuguese glass-packing production company for food and beverages. Headquartered in Avintes, Vila Nova de Gaia, the company ensures an annual production of more than 11 billion containers distributed to over 80 countries worldwide. Originally incorporated as Barbosa & Almeida, the company started in 1912 dedicated only to the commercialisation of bottles. In 1930, the industrial glass manufacturing activity started.

After years of technological development, the geographical expansion took place. In 1993, a glass company was bought in Marinha Grande, Portugal. In 1998, the first abroad factory unit was constructed, in Villafranca de los Barros, Spain. The following year, a factory unit was bought from another company in Léon, also in Spain. In 2012, the Polish group Warta Glass was bought, marking the first expansion to Eastern Europe. The expansion to central Europe was marked by a German glass packaging company acquisition in 2016. In 2017, the company acquired four extra factory units from the Yioula Group: one in Greece — Athens, one in Romania — Bucharest, and two in Bulgaria — Sofia and Plovdiv. Since then, the company has had a total of 12 factories, distributed in 7 countries.

Along with its expansion, BA Glass has perfected a business model inspired by the group's values (HeART - Humility, Ambition, Rigour and Transparency, with emotion) based on permanent innovation and internal entrepreneurship. The company has almost 4000 employees and a turnover of more than 1010 million euros [1].

BA Glass joined the Porto Protocol, launched in 2018, committing to a lower use of natural resources and the protection of the environment. In 2021, the company also joined the Science-Based Targets initiative, looking for an establishment of ambitious science-based emissions reduction targets. Furthermore, for the second year in a row, BA Glass was recognised as the Most Sustainable Company in the Glass Industry by the World Finance Sustainability Awards, in 2021. In the same year, was also presented with a Gold rating from Ecovadis, a business sustainability rating index [1].

1.3 Objectives

The main objective of this thesis is to develop a mathematical model in order to calculate the power transferred to the melted glass through the electrical boosting system of an actual glass-melting furnace. The developed mathematical model considers the temperature and chemical composition of the melted glass, the dimensions of the furnace and its electrical boosting system, and the operational parameters. Academic publications and books are the main knowledge source.

Furthermore, this study has the purpose of presenting a better theoretical understanding of the electrical boosting operation, namely the power distribution in the glass melt and its effects on the glass quality. Not only, but it will also look for insights into efficiency, creating new room for improvement in energy consumption.

1.4 Thesis Outline

This Thesis is composed of 5 chapters, of which the first chapter is the introduction. This chapter provides the framework of the research, the company description, the objectives and the methodologies applied, in addition to this description of the thesis structure.

Chapter 2 provides a theoretical foundation through the state-of-the-art, where the glass-making process and the importance of electrical boosting are explained, and studies related to this topic are presented.

Chapter 3 contains the materials, such as operational and dimensional parameters, and the methods, namely the programs used and the calculations performed.

Chapter 4 consists of the results of the study and its respective discussion.

Finally, Chapter 5 presents a synthesis of the results obtained in the previous chapter, followed by some development proposals for future work to improve the results and the conclusions obtained in this work.

Chapter 2

State-of-the-art

Glass is an elastic, hard, transparent material, that presents electrical, chemical, and thermal resistance [2]. It has been present in society for thousands of years, with the first records from 7000 B.C. [3]. Throughout human history, it has played important roles in a wide range of products, being considered one of the most powerful and influential materials [2–4].

An actual and improved scientific definition was developed by Zanotto and Mauro, considering glass as a non-equilibrium, non-crystalline state of matter that appears solid on a short time scale but continuously relaxes towards the liquid state [5].

2.1 Glass-making Industry

Glass manufacturing plants have an intense demand for energy due to the requirement to heat up the raw materials, melt, refine and keep the glass at a constant temperature, around 1550 °C or even higher, depending on the sort of glass produced. It was estimated that this process consumes around 5-7 GJ per ton of glass produced [6]. At the moment, the 2255 furnaces constructed, displayed in 92 countries, combine an installed capacity of 222 million tons of glass per year [7]. In Europe, around 160 glass manufacturing plants, distributed in over 20 countries, produces around 80 billion bottles, jars and flacons each year [8]. Among the leaders of the market, it is Ardagh Group, based in Luxembourg, this company has a revenue of close to 9 billion dollars [9].

Glass production can be categorized by the sort of glass produced, obtaining five major sectors [3]:

- Flat glass: windows, automobile windshields and picture glass;
- Container glass: bottles, jars and packaging;
- Pressed/Blown glass: light bulbs, scientific and medical glassware, flat panel display glass;
- Glass fibre: fibreglass, optical fibres;
- Products from purchased glass: items assembled from intermediate glass products, such as aquariums, mirrors, and table tops.

Another common categorisation for glasses is related to their composition. This categorisation allows grouping the glasses with similar physical, chemical and thermal properties, as presented below [10]. Figure 2.1 displays different sorts of glasses.

- Vitreous silica: very high electrical resistivity, low thermal expansion coefficient, resisting temperatures above 1000 °C, and optical transparency over a wide spectral range (e.g. optical fibres, ultraviolet and infrared transmitting optics);
- Soda-lime-silica (SLS) glasses: similar properties as the vitreous silica, but with a melting temperature around 500 °C lower (e.g. flat and containers glasses, incandescent lamps, domestic glass);
- Borosilicate glasses: thermal shock resistance and excellent chemical durability (e.g. Pyrex®, flat panel display glass, fluorescent lamps, chemical laboratory ware);
- Glass fibres: divided into two main subcategories, common thermal and sound insulation fibres, and high-value fibres used in more extreme thermal environments (e.g. optical fibres, fibreglass cloth);
- Television tube glasses: a higher level of heavier ions are found, to create protection against radiation (e.g. television and other cathode ray tubes);
- Glass-ceramics: very strong and thermal shock resistant (e.g. cookware, electric stove tops, telescope mirrors);
- Other commercial glasses: wide range of composition possibilities, and subsequently, properties possibilities (e.g. optical lenses, dental restorations, mirrors).



Figure 2.1: Soda-lime-silica (flat glasses on the left side, container glasses on the right side) and borosilicate glasses (laboratory glassware, in the middle), adapted [11–13].

Different methods can be used to melt and produce glass, mainly depending on the sort and amount desired. Batch (discontinuous), semi-discontinuous and continuous production are the three options for the glass melting process. For any of these options, batch preparation is important, where the raw materials are ground and blended to obtain the ideal mixing composition [14].

In the case of container glasses, based on soda-lime-silica composition, not only the melting process is continuous, but the whole production system. Figure 2.2 represents the process. It starts with batch preparation, detailed above.

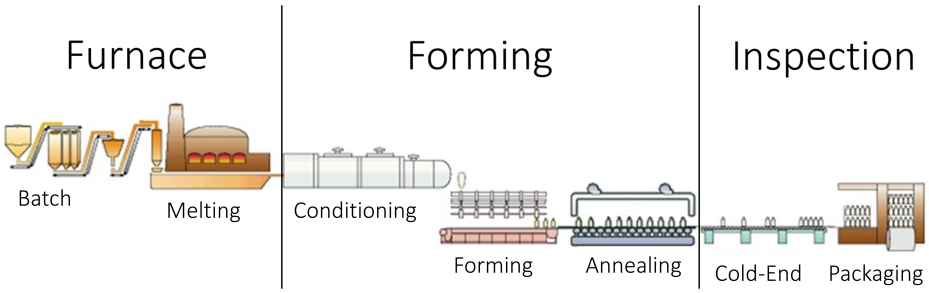


Figure 2.2: Glass Container Production Process, adapted [15].

Continuous glass furnaces, also known as glass-melting tanks, are the furnaces where the raw materials go through fusion, while constantly fed with mixed batches. These furnaces are responsible for reaching the desired residence time and, subsequently, the quality standards. It is important to mention that this method, besides being able to mass-produce glass, is also suitable for most of the types of glasses mentioned above. A traditional glass-melting furnace consists of 6 parts [14]:

- Doghouse: connected to the batch silos, it feeds the melting tank continuously with raw material. It can be located at the beginning or on the sides of the furnace;
- Melting tank: typically has three sections — melting and reactions, dissolution, and refining. For the melting and reactions, temperatures are commonly around 1000–1300 °C, while 1400–1550 °C offers good homogenising and refining for the other remaining sections [16]. The residence time usually ranges from 24 to 30 hours [15];
- Combustion chamber: also known as the superstructure, is the volume on top of the melting tank where the natural gas combustion happens. It can be cross-fired (combustion from the sides) or end-port-fired (combustion from the beginning). Air-fired are more common but can be found in oxygen-fuel cross-fired combustion chambers.
- Heat exchangers: crucial for energy savings, they can be either recuperative or regenerative. A recuperative heat exchanger preheats the combustion air through a recuperator, exchanging heat from the hot flue gases. A regenerative one has two regenerator chambers with refractory bricks stacked where, while the hot flue gases are heating one up, the other is transferring the heat accumulated from the previous cycle to the combustion air;
- Throat: responsible for passing the melted glass from the end of the melting tank to the working chamber. Here is where the furnace section ends and the forming one starts;
- Working chamber: usually known as forehearths, its main function is to condition the glass at the required temperature to be delivered to the forming process. At the end of the forehearth, there is a feeder mechanism that produces a regular flow of gobs with a constant shape and weight [15].

For the refining section, mentioned above, it is possible to install mechanisms to assist and improve the process, such as bubbling, that promotes mechanical agitation by injecting air through bubblers and creates an actual barrier for the unmelted glass, ensuring enough residence time. Another possibility is electrical boosting, which boosts the energy introduced in the system by the passage of an electric current between the electrodes inserted in the melt, resulting in Joule heating.

It is presented below, in Figure 2.3, a representation of a glass-melting tank, end-port fired. It is relevant to mention that inspection ports can be found on the sides, to allow visual inspection of the interior.

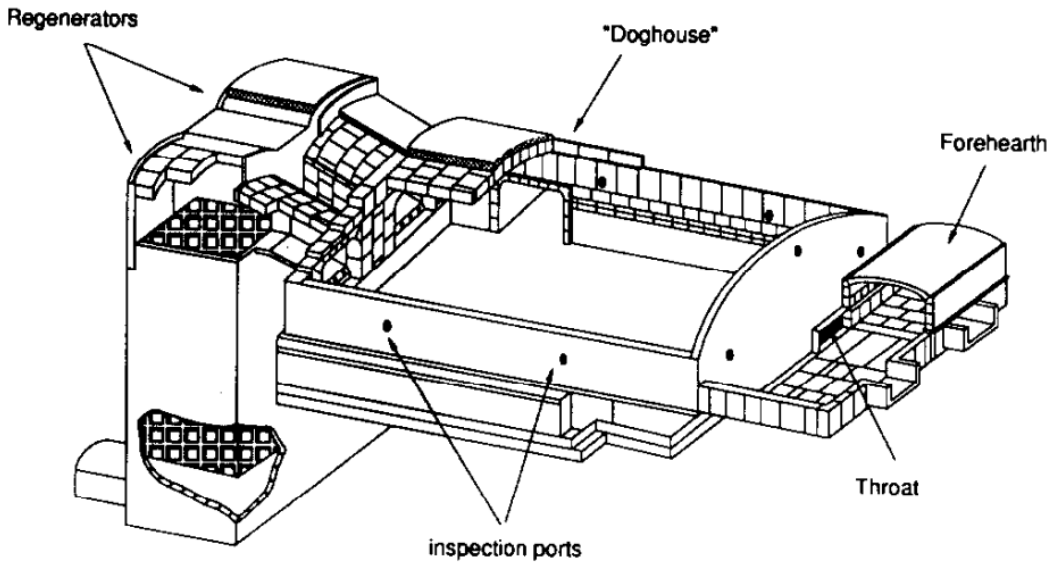


Figure 2.3: Representation of an end-port fired furnace [17].

Continuing the forming section, the gobs produced by the forehearths are loaded into the moulds where, by blowing process, it obtains the desired container shape. There are 3 different blowing methods: Blow & Blow, Press & Blow and Narrow Neck Press & Blow. At this stage, the glass temperature drops from 1150–1200 °C to 600–650 °C in about 10–25 seconds [15]. After the bottles are formed, they are heated up to the annealing temperature for a specific amount of time and slowly cooled down, towards release the internal stresses created by the abrupt change of temperature in the blowing process. Although it is similar to the cold-end name, a cold-end treatment takes place as the last part of the annealing part, helping to protect and lubricate the bottles, avoiding damage or marks during the remaining process and its life cycle.

The inspection is the last section of the glass container production process, composed of the cold-end and packaging. At the cold-end, there are inspection machines that assure dimensional and aesthetical parameters for all the bottles produced. Finally, the packaging consisted of stacking the bottles in layers on pallets, to then storage in the warehouse.

2.2 Glass Composition

Having a melting temperature of around 1500 °C, the ternary system *soda-lime-silica*, with the addition of other oxides, drives the production costs to values lower than vitreous silica glasses, maintaining the desired properties. Besides keeping the capacity of producing glasses on a large scale, the soda helps to decrease the melting temperature, decreasing the chemical durability of the glass. To compensate for that, the called limestone, scientifically known as calcium oxide (CaO) is added, increasing the chemical durability [10]. An equilibrium is needed between these components. Table 2.1 displays the typical composition range for SLS glasses. Minor components were not included.

Table 2.1: Typical SLS glass composition range, adapted [18]

Weight (wt%)	Container	Float	Domestic
SiO_2	70–73	70–74	70–74
Na_2O	12–15	12–14	12–14
CaO	10–12	7–10	7–9
Al_2O_3	1–2	0–1	1–2
MgO	0.5–2	2–4	1–2
K_2O	0–1	0–0.5	0–2.5
SO_3	0–0.5	0–0.5	0–0.5
Fe_2O_3	0–1	0–1	0–0.05
TiO_2	0–0.1	0–0.1	0–0.05
Cr_2O_3	0–0.3	0–0.3	0

Container glasses can be produced in several different colours. White container glass represents half of the world's production, while brown amber and green, are about one-quarter each. Mainly, green colour is achieved by adding chromium and iron, amber colour can be made by lower sulfur levels and higher iron levels, when compared to the white colour. Each colour has its own variation, such as light green, coloured using iron only [19]. The average composition of white, green and amber container glass is shown in Table 2.2.

Table 2.2: Average container glass composition by colour, adapted [19]

Weight (wt%)	White	Green	Amber	Average
SiO_2	72.28	71.21	71.75	71.75
Na_2O	13.47	13.37	13.83	13.55
CaO	9.69	9.30	9.30	9.45
Al_2O_3	1.83	2.28	2.03	2.05
MgO	1.60	2.27	1.98	1.95
K_2O	0.54	0.74	0.57	0.62
SO_3	0.21	0.13	0.02	n/a
Fe_2O_3	0.09	0.36	0.26	n/a
$R'O$	11.36	11.56	11.30	11.40
R_2O	14.00	14.00	14.39	14.17
Nº of analyses	67	57	55	179

Regarding energy requirements, although the theoretical minimum specific energy consumption (SEC) for this class of glass is between 2.3 to 2.6 GJ per tonne of the raw batch, the average SEC operated is close to 5 GJ per tonne. These values are close to the ones for glass in general, as mentioned before. Cullet is added to the batch since it can reduce the specific heat consumption required for the melting by 0.3 % for every 1 % cullet added [18].

2.3 Electrical Properties

Electrical boosting, mentioned in Section 2.1, is a technology based on direct resistance heating, where electrodes are immersed in the glass, connected to a transformer and a power supply that provides an electric current then, by Joule heating, releases energy directly into the glass. It is notable that different from combustion, a process based on indirect gas heating with high heat losses from the combustion chamber and the residual waste gases, the electric boosting system presents fewer losses potentials in the process [20]. Since the glass, at higher temperatures, presents values of resistivity of a semiconductor, it is still able to conduct electrical current and generate a reasonable amount of energy by its resistivity. Usually, an electrical boosting system is composed of a three-phase transformer, cables and busbars, electrodes and its control panel.

Lately, it has increased its value in the glass industry, not only by helping to achieve the desired quality standards but also by reducing the atmospheric pollution of the process. This technology offers easy control of the system, high thermal efficiency, and provides better convection currents and homogeneous glass production [21]. It is crucial to study and project an optimal electrical boosting system, considering the number of electrodes, its measurements (diameter, length, immersion, spacing), avoiding convection currents in the wrong places or offering a shortcut flow path that decreases the residence time [20].

Sidewall or bottom, barrier and throat electrodes are the three different positionings found nowadays. Usually set in end-port furnaces, electrodes are installed horizontally on the side walls and on the beginning of the furnace, below the burner port. Each position depends only on the dimensions of the furnace. Another possibility is to install vertical electrodes on the bottom of the furnace, where the efficiency is higher than the side walls, due to a balanced current and heating distribution. A barrier booster system is characterised by a row of electrodes positioned at the bottom of the furnace, perpendicular to the flow path, usually near the hot spot. This design intensifies the upward convection current, bringing cold glass from the bottom to the surface, where the combustion completes the heating process. A throat booster has the objective to direct heat to a particular area that would be hard to heat in conventional operation conditions, such as the throat and the riser of the furnace [22]. Figure 2.4 below presents a side wall positioning.

The electrical boosting can be used either as a share of the melting power, working together with combustion, or as the only melting power, in the case of a full-electric furnace. Currently, in container glass production, the boosting share can be up to 25 % of the melting power. A furnace with a 25 % share of electrical boosting saves up to 17 % energy when compared to a furnace with no electrical boosting [20]. The share of electrical boosting operation is typically

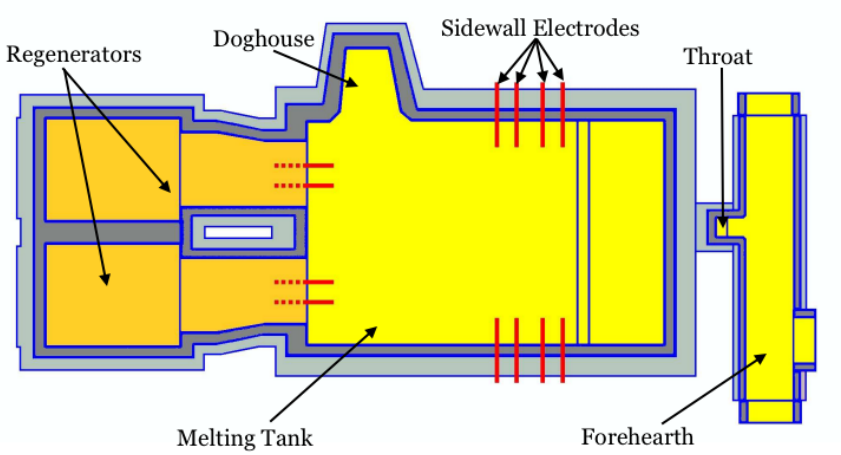


Figure 2.4: Representation of a sidewall boosting system for an end-port fired furnace, adapted [22].

not related to natural gas and electricity prices, as the impact of their share changes requires a certain adaptation time to stabilise the production. Instead, it primarily relies on the requirements for convection currents and localised heat dissipation [15]. Analyzing both extremes, fossil fuel-fired furnaces, with no electric boosting share, have an efficiency of around 45 %, meanwhile, an electric furnace, with the same dimensions has an efficiency of up to 85 %. It is known that every 5 % increase in boosting share, reduces around 3.5 % the emission of carbon dioxide per ton of glass [23].

Although it appears to be a promissory option compared to traditional combustion furnaces, all-electric furnaces have a shorter lifetime (2 to 7 years, while 10 to 20 years for traditional ones). Furthermore, a stable and reliable power grid is required, and while it is not supplied by renewable sources, its environmentally friendly aspect is not established with a higher carbon footprint [24].

2.3.1 Electrical Resistance

Joule heating, also known as the Joule effect, is the conversion of electric energy into thermal energy. The electrical current applied passes through the melt driven by a voltage gradient, and due to its electrical resistivity, generates and dissipates the heat in the melt. Although it is a very used technology in the glass industry, there are not many studies presenting and explaining how to simulate and calculate the electrical resistance and its real energy contribution to a glass-melting tank.

A study developed by Curran [25], using a a lumped parameter network-type thermal analyser computer program, concluded that the power density at the surface of the electrode is around 20 times higher than a short distance from the electrode, where it gets uniform and stable. More recent studies were found regarding more complex computer simulations which take into account the electrical boosting system on glass furnaces. However, these studies do not demonstrate how the calculations were performed.

Durubal [26] conducted a comprehensive study on an oxygen-fired unit melter, utilising an advanced mathematical model. The primary focus of the research was to optimise the positioning of electrodes within various sections of the glass-melting tank. This investigation aimed to determine the power distribution and resulting temperature increase for different scenarios, carefully considering the impact of convective currents and temperature profiles. The outcomes of the simulations led to a significant finding: a strategically positioned boost system effectively enhances convection currents, thereby increasing the desired effects of top firing. As a result, the average furnace temperature rises, ensuring a continuous and smooth glass flow pattern.

Li et al. [27] used an integrated glass furnace model of combustion space and glass tank to study a float glass furnace with an electrical boosting system. The applied mathematical model considered several sub-models, such as combustion, radiation, turbulent, glass tank, glass flow, batch blanket, and electric model. For the electric model, it was considered an electric potential field generated between the electrodes in the melt, and calculating the power dissipated by Joule heating. By the performed simulation, it was possible to conclude that the electrical boosting prolongs the lifetime of the glass furnace. A shorter minimum residence time can also be achieved.

A similar and more complex study was performed by Raič et al. [28], which also considered many of the different sub-models presented in the study above, with a CFD simulation of an oxy-fuel glass melting furnace, considering similar assumptions from Li et al. [27]. For the electric boosting modelling in the glass tank, the electric power input was solved by an electric potential equation in fluid simulation software.

More outdated studies presented not as complex information about the operation and theoretical expectations of this technology, such as Staněk, which affirms that the transfer of electrical to thermal energy through electric current is very high, ranging around 90 % or even higher [21]. In the industry, it is expected an efficiency between 80 % and 90 % (information provided by supplier companies). Another study developed by Staněk estimated that 89 % of the effective power was dissipated within 3 electrode diameters distance [29].

Gruenberg performed an experimental physical model of a water bath in a plastic tray using copper electrodes. By establishing the electric current through the bath and having a pair of meter probes separated by a constant distance, it was possible to conclude that between 85 % and 92 % of the total power is dissipated in 8 % of the melting-tank area [30].

When the electrical boosting system is constructed with rods, the power dissipation is nonuniform. It happens due to a lower resistivity of the hotter glass near it and the proximity to each other, tending to concentrate the current and energy dissipation at the tips. Not only, corrosion at the tips of horizontal rods can also happen due to these factors [31].

Chapter 3

Methodology

The following sections will provide a comprehensive overview of the materials utilised, experimental procedures carried out, and data analysis techniques employed. It is important to note that the methods chosen were carefully selected to address the research objectives and were implemented with meticulous attention to detail and accuracy. By outlining the methods and techniques utilised, this chapter allows for the critical evaluation and replication of the research.

3.1 Furnace Data

In this section, it will be presented a detailed description of the typical furnace layout along with its operational parameters, providing the essential data required for subsequent calculations. Any assumptions made during the study will also be thoroughly discussed.

3.1.1 Furnace Layout

As mentioned in Chapter 2, the furnace is composed of several parts. In this study, only the melting tank and its accessory, the electrical boosting system, will be relevant. In the following two subsections, the dimensions for the melting tank and electrical boosting are presented.

3.1.1.1 Melting Tank Dimensions

The melting tank has a rectangular shape, with 16.002 m of length, 8.534 m of width and 1.524 m of height. However, to ensure precision and control, a minimal space of 0.076 m is intentionally maintained between the glass melt surface level and the tank's uppermost edge. Consequently, the effective height of the glass melt within the tank measures 1.448 m, guaranteeing optimal conditions for the melting process.

3.1.1.2 Electrical Boosting Dimensions

The electrical boosting system is fed by a three-phase Varivolt transformer, an on-load step-less variable voltage transformer, that work from 30 to 30 000 kVA. With this equipment, it

is possible to feed each phase with the exact desired voltage, providing up to 5000 A of electric current. Each phase is connected to four horizontal rod electrodes, totalling 12 electrodes inside the melting tank. Each electrical phase has two terminals, composed of two electrodes each. Between the same terminals electrodes, there is no voltage gradient. The main voltage gradient is found between terminals from different phases. A voltage gradient can be also found between same-phase terminals.

The display of the electrodes is presented below in Figure 3.1. The electrodes are made of molybdenum, where each electrode has a length of 0.600 m and a diameter of 0.062 m.

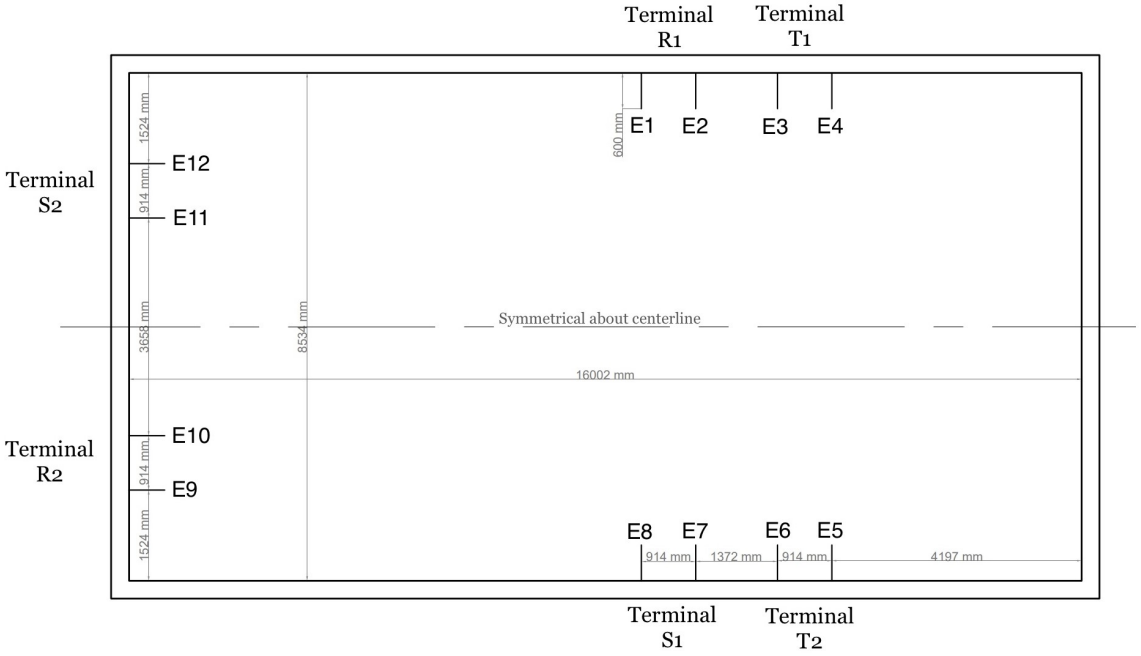


Figure 3.1: Representation of the electrical boosting system in the furnace and its measurements.

As presented in the figure above, the electrodes are named from E1 to E12. The electric phases are named on the RST system, where R stands for Reference, S for Secondary and T for Tertiary phase. Phase R supplies the electrodes E1, E2, E9 and E10, while phase S supplies the electrodes E7, E8, E11 and E12, and phase T, the electrodes E3, E4, E5 and E6. The electrodes from each phase are divided into terminals: on phase R, terminal R1 stands for electrodes E1 and E2, R2 for E9 and E10; on phase S, S1 stands for E7 and E8, S2 for E11 and E12; on phase T, T1 stands for E3 and E4, T2 for E5 and E6. Each pair has a voltage-to-ground measurement device, with the values later presented.

Depending on the electrode, the height which is installed is different. For the electrodes E1 and E8 to E12, its height it is 0.444 m. The electrodes E2 and E7 are installed at 0.549 m of height. The electrodes E3 and E6 are at a height of 0.699 m, while the electrodes E4 and E5 are at 1.024 m. Considering these heights and the distance presented in the figure above, it is possible to determine the distance between each pair of electrodes from different terminals. The calculation of the distance (b_{ik}) between the electrodes considers the measurement from the electrode's tip to

the other's tip, taking into account both the vertical and horizontal placements. The distances are presented in Tables B.1 and B.2, on Appendix B.

It is important to mention that despite the electrodes having an initial length and diameter, erosion and corrosion may happen and change their dimensions [29]. For this study, all the electrodes were considered under their initial conditions.

3.1.2 Operational Parameters

The glass melt composition is obtained from BA Glass proprietary recipes. The remaining operational parameters, namely the glass melt temperature and the ones from the electrical boosting system, were obtained from internal software, used by the company to operate the glass melting production. It is important to mention that the furnace and its electrical boosting system operate in a continuous mode.

3.1.2.1 Glass Melt Composition

For the SLS glass melt composition, the composition values from the internal recipe selected are presented below. Due to confidentiality, only the three main components were presented in Table 3.1, with a simple rounding. The remaining components are presented without their composition. Regarding its density and specific heat at constant pressure, both at 1550 ºC, the values assumed in this work will be 2500 kg m^{-3} and 1.330 kJ kg^{-1} $^{\circ}C^{-1}$, respectively.

Table 3.1: Chemical composition of the glass melt for the 4 scenarios

Component	Composition (mol%)
SiO_2	72
Na_2O	12
CaO	11
Al_2O_3	Confidential
K_2O	Confidential
MgO	Confidential
Fe_2O_3	Confidential
SO_3	Confidential
Cr_2O_3	Confidential
$R'O$	Confidential
R_2O	Confidential

3.1.2.2 Glass Melt Temperature

Due to the conditions of the thermocouple installed in contact with the glass melt, it is not possible to determine its exact temperature. Once it is known that the temperature works in a short range, the temperature of 1550 ºC is considered as the temperature of the glass melt, being this option selected as the best one to overtake this situation. Also, due to the lack of information about

the exact temperature profile for this furnace, it was considered that the melt is homogeneous, presenting the same temperature at any position.

3.1.2.3 Electrical Boosting Parameters

The electrical boosting parameters can be presented per phase or per electrode. The parameters from each phase are the ones listed below, where the subscripts R, S and T refer to each phase, and R1, R2, S1, S2, T1 and T2 refer to each terminal, as presented in Subsection 3.1.1.

1. Theoretical Power (kW) — $P_{t,R}$, $P_{t,S}$, $P_{t,T}$;
2. Phase Voltage (V) — U_R, U_S, U_T;
3. Voltage to Ground for each terminal (V) — U_{R1}, U_{R2}, U_{S1}, U_{S2}, U_{T1}, U_{T2};
4. Electric Current (A) — I_R, I_S, I_T.

Besides the ones above, the only parameter given per electrode is the Electrode Current (A) — I_{e_i}, for the i^{th} electrode. Tables 3.2 and 3.3, presented below, display all the values of the parameters mentioned above, for different days of production. It is important to mention that the days considered were corresponding to the recipe selected.

Table 3.2: Electrical boosting parameters for 4 different days of production

Phase	Parameters	Scenario 1	Scenario 2	Scenario 3	Scenario 4	Units
R	U_R	159	152	162	165	V
	U_{R1}	93	87	94	91	V
	U_{R2}	66	65	68	74	V
	I_R	2068	2042	2076	2148	A
	$P_{t,R}$	318	300	325	343	kW
S	U_S	181	174	182	187	V
	U_{S1}	90	86	89	91	V
	U_{S2}	91	88	93	96	V
	I_S	1868	1797	1851	1900	A
	$P_{t,S}$	328	300	325	342	kW
T	U_T	250	247	246	250	V
	U_{T1}	100	100	98	97	V
	U_{T2}	150	147	148	153	V
	I_T	3648	3660	3546	3615	A
	$P_{t,T}$	908	900	868	900	kW

Table 3.3: Electric current on each electrode for 4 different days of production

Phase	Electrode	Scenario 1	Scenario 2	Scenario 3	Scenario 4	Units
R	E_1	907	945	894	911	A
	E_2	1172	1214	1159	1175	
	E_9	940	1000	945	959	
	E_{10}	1134	1154	1100	1122	
S	E_7	991	1019	965	984	A
	E_8	931	938	892	924	
	E_{11}	1014	1035	972	1014	
	E_{12}	859	870	829	842	
T	E_3	1859	1866	1873	1824	A
	E_4	1801	1761	1797	1733	
	E_5	1856	1829	1866	1775	
	E_6	1808	1802	1808	1787	

It is important to note that the values presented in Tables 3.2 and 3.3 are subject to an unknown level of imprecision. Since these values are primarily used for operational purposes, a certain degree of imprecision is expected. This is evident from the absence of decimal places in all the values. Consequently, this imprecision can directly influence the values of effective power dissipation and efficiency. In order to consider the mentioned imprecision, a sensibility analysis is performed, further presented. Additionally, if the electrodes were in perfect conditions, as mentioned previously, it would be expected that the electric current values for each pair of electrodes should be identical.

Besides the values presented above, the electrode temperature is also an important parameter. On average, for phases R and S, the electrode temperature is about 500 ºC, and for phase T, 600 ºC. At each temperature, the molybdenum has a resistivity of $9.2 \cdot 10^{-7}$ and $11.0 \cdot 10^{-7}$ Ω m, respectively [32]. Then, the electrode resistivity is represented by ρ_e and has the previous values, depending on the phase.

3.2 Methods

Initially, two distinct models are employed to calculate the electrical resistivity. Subsequently, the resistance is determined, taking into account the dimensions of the furnace and the resistivity values obtained. This study aims to evaluate the conversion of electrical energy into heat energy. Therefore, it does not consider the assessment of energy losses as heat after the conversion has already taken place. Furthermore, it encompasses calculations related to power dissipation and heat transfer. Notably, the analysis considers a steady-state condition of the furnace and no fluid dynamic effects.

In the context of this study, it is of utmost significance to highlight that the exclusion of electrical mismatch was a deliberate decision made for academic reasons. As a result, the calculations for phase voltage were performed utilising arithmetical computations, instead of vectorial ones.

3.2.1 Resistivity Model

Once the layout parameters are not going to change significantly, even if considered any sort of wear, the initial step is to define the electrical resistivity. The electrical resistivity, or specific resistance, is the capacity of a certain material to resist the flow of electricity [33]. It is measured as Ω m, but also can be found as Ω cm.

Some glass properties, such as viscosity and electrical resistivity, depend on the chemical composition and temperature. These properties can be approximated by using the Vogel-Fulcher-Tamman (VFT) equation, presented below, after measuring the properties experimentally at a certain temperature interval, fitting it to the parameters and then interpolating using the equation (as well, it is possible using fixed temperatures instead of a temperature interval) [34]. Usually, a relation is developed for a specific sort of glass, due to different composition ranges in the industry.

$$\rho = \exp\left[C + \frac{B}{T - T_0}\right] \tag{3.1}$$

For this equation, ρ is the electrical resistivity (Ω m), T is the temperature (°C), and B, C and T_o are composition-dependent parameters. The logarithmic scale is crucial for obtaining absolute error, instead of a relative one [35]. The composition-dependent parameters can be expended to a linear function of the i^{th} component mole percent x_i, [34]:

$$\ln\rho = \sum_{i=1}^{n} C_i x_i + \frac{\sum_{i=1}^{n} B_i x_i}{T - \sum_{i=1}^{n} T_{0,i} x_i} \tag{3.2}$$

where n is the number of components.

Until the end of the 1950s, only very simple methods to calculate the glass melt electrical resistivity were developed, not considering all the components capable of influencing the resistivity [36]. Later, different modelling was developed for different ranges of temperature and glass composition [18]. In the literature, most glass melt resistivity studies and values are summarised by Varshneya et al. [37], Mazurin et al. [36] and Fluegel et al. [35].

Varshneya et al. [37] published experimental measurements of 6 different families of glass compositions for high-temperature melts. For SLS glasses, a second-order model was developed by Mazurin et al. [18, 36], and a third-order model by Fluegel et al. [35]. Both models consider the chemical composition as a molar percentage (mol%). Different from the theoretical Equations 3.1 and 3.2 presented above, described above, the models are based on $\log_{10}\rho$ instead of $\ln\rho$.

It is also noticeable that in both models, values obtained for T_0 were non-physically meaningful predictions [36]. However, these models are only used for electrical resistivity data in a certain high-temperature range [35]. Also, the original studies did not provide any units for the VFT coefficients for both models. Therefore, no units were assumed in the following coefficients calculations.

3.2.1.1 Mazurin Model

This second-order model was constructed to calculate the electrical resistivity of commercial SLS melts, ranging from 600 °C and 1400 °C. Initially, it is necessary to calculate the resistivity at 600 °C, 900 °C and 1300 °C. After that, the VFT-related constants are calculated. Once the VFT equation is constructed, it can be used to determine the electrical resistivity at any temperature inside the stated range, [36]. For this model, besides comparison with other studies, no data was found about its confidence interval or other statistical indicators.

Although, it is applicable only for a certain compositional range, presented on the Table 3.4 below. The $R'O$ represents the sum of calcium oxide (CaO) and magnesium oxide (MgO), and the R_2O, the sum of sodium oxide (Na_2O) and potassium oxide (K_2O) [36].

Table 3.4: The applicable compositional range for Mazurin model, adapted [36]

Component	Range (mol%)
SiO_2	69–81
Na_2O	12–20
K_2O	0–7
CaO	4–15
MgO	0–5
Al_2O_3	0–4.5
$R'O$	4–15
R_2O	12–20

In detail, to perform the calculations, the following three steps need to be done:

1. Calculate the electrical resistivity $\log_{10}\rho\ (\Omega\ cm)$ for each temperature (T = 600 °C to obtain ρ_{600}, T = 900 °C to obtain ρ_{900}, T = 1300 °C to obtain ρ_{1300}), for a given composition, using the coefficients presented on the Table A.1, on Appendix A.

$$\log_{10}\rho = \beta_o + \sum_{i=1}^{n}\left(\beta_i\, x_i + \sum_{k=i}^{n}\beta_{ik}\, x_i\, x_k\right) \tag{3.3}$$

where β_o is the intercept, β_i and β_{ik} are the i^{th} component first-order coefficient, and the ik^{th} component second-order coefficient, respectively. The same applies to the component mole percent x_i, x_{ik}. The n represents the number of significant components.

2. To construct the Vogel-Fulcher-Tamman equation, the following constants need to be calculated:

$$M = 400\ (\rho_{600} - \rho_{1300}) \tag{3.4}$$

$$N = 700\ (\rho_{900} - \rho_{1300}) \tag{3.5}$$

$$T_0 = \frac{(873\ M - 1173\ N)}{(M - N)} \tag{3.6}$$

$$B = \frac{(\rho_{900} - \rho_{1300})\ (1573 - T_0)\ (1173 - T_0)}{400} \tag{3.7}$$

$$C = \rho_{600} - \frac{B}{873 - T_0} \tag{3.8}$$

It must be mentioned that no units were found for the coefficients M, N, T_0, B and C in the original studies.

3. Finally, it is possible to determine the electrical resistivity $\log_{10}\rho$ (Ω cm) at any given temperature T (between 600 ºC and 1400 ºC) for a certain melt composition:

$$\log_{10}\rho = C + \frac{B}{(T - T_0)} \tag{3.9}$$

where T is given in ºC.

3.2.1.2 Fluegel Model

Although it presents a similar structure to the one presented above, this third-order model is suitable for a higher number of components (without an explicit limit for the composition range) and also considers even more component interactions, such as ternary systems. This model is set to operate for a temperature range between 1000 °C and 1400 °C.

Moreover, this model used more than 300 data points for each temperature (1000 ºC, 1200 ºC, 1400 ºC), obtaining a coefficient of determination of 0.9957, 0.9953 and 0.9878, and a degree of freedom of 274, 289 and 284, respectively. It can also be used as an electrical resistivity calculator to determine the confidence interval [38].

In detail, to perform the calculations, the following three steps need to be done:

1. Calculate the electrical resistivity $\log_{10}\rho$ (Ω cm) for each temperature (T = 1000 °C to obtain ρ_{1000}, T = 1200 °C to obtain ρ_{1200}, T = 1400 °C to obtain ρ_{1400}), for a given composition, using the coefficients presented on the Table A.2, on Appendix A.

$$\log_{10}\rho = \beta_o + \sum_{i=1}^{n}\left(\beta_i\ x_i + \sum_{k=i}^{n}\left(\beta_{ik}\ x_i\ x_k + \sum_{m=k}^{n}\beta_{ikm}\ x_i\ x_k\ x_m\right)\right) \tag{3.10}$$

where β_o is the intercept, β_i, β_{ik}, and β_{ikm} are the i^{th} component first-order coefficient, the ik^{th} component second-order coefficient, and the ikm^{th} component third-order coefficient, respectively. The same applies to the component mole percent x_i, x_{ik}, x_{ikm}. The n represents the number of significant components.

2. To construct the Vogel-Fulcher-Tamman equation, the following constants need to be calculated:

$$T_0 = 200\ \frac{7\ \log_{10}(\rho_{1400}) + 5\ \log_{10}(\rho_{1000}) - 12\ \log_{10}(\rho_{1200})}{\log_{10}(\rho_{1400}) + \log_{10}(\rho_{1000}) - 2\ \log_{10}(\rho_{1200})} \tag{3.11}$$

$$B = \frac{(\log_{10}(\rho_{1000}) + \log_{10}(\rho_{1200}))\ (T_0 - 1000)\ (T_0 - 1200)}{200} \tag{3.12}$$

$$C = \frac{B + \log_{10}(\rho_{1200})\ (T_0 - 1200)}{T_0 - 1200} \tag{3.13}$$

3. Finally, it is possible to determine the electrical resistivity $\log_{10}\rho$ (Ω cm) at any given temperature T (between 1000 ºC and 1400 ºC) for a certain melt composition:

$$\log_{10}\rho = C + \frac{B}{(T - T_0)} \tag{3.14}$$

where T is given in ºC.

3.2.2 Resistance Calculation

Either for wires or flat electrodes, the glass electrical resistance can be defined by the following conventional equation [39]:

$$R = \rho\frac{L}{A} \tag{3.15}$$

where ρ is the electrical resistivity (Ω m), A is the surface area (m^2) of flat parallel electrodes (or the cross-sectional area of a wire) and L is the distance (m) between electrodes (or the length of the wire).

In the case of horizontally placed electrodes, as the side wall design mentioned above, the equation would be adapted to the layout and dimensions of the electrodes [21, 40]. Different equations can be found in the literature, for different furnace and electrode geometries [41]. In the most recent one, published in 1986, Staněk [21] presented an equation that takes into consideration the distance b_{ik} between each pair of electrodes i and k. As mentioned above, the distances b_{ik} between each possible pair used are presented in Tables B.1 and B.2, in Appendix B. For the same pair of electrodes i and k, it is calculated the effective resistance, R_{ik}, once the resistivity is calculated from each model:

$$R_{ik} = \frac{\rho}{\pi l}\ \ln\frac{2b_{ik}}{d} \tag{3.16}$$

where l is the length of the electrode (m), d is the diameter of the electrode (m), which is the same for all electrodes, and b is the distance between the electrodes (m).

It is notable the relation between Equations 3.15 and 3.16, where the second one presents a natural logarithmic distance and diameter but maintains the concept of the equation. In the second equation, the cross-sectional area is expressed by the longitudinal area of the cylinder, considering the natural logarithmic diameter. In other words, it considers, in a simplified form, that there is a wire of length $\ln b_{ik}$ and a cross-sectional area of $\pi\ (l \cdot \ln \frac{d}{2})$, with a resistivity ρ, where the electric current passes through.

It is important to mention that this equation, originally developed for parallel electrodes, was extended to calculate the resistance between non-parallel electrodes for academic purposes. The extension was necessary as no equation specifically developed for non-parallelly immersed electrodes was found in the existing literature.

The effective power represents the power introduced into the melt. When considering electrodes in an electrical boosting system, the effective power $P_{u,\ ik}$ of the electrode pair combination is obtained after calculating the resistance R_{ik} between the electrodes i and k (Ω), as presented above, and considering the voltage differential from the electrode pair:

$$P_{u,\ ik} = \frac{|U_i - U_k|^2}{R_{ik}} \tag{3.17}$$

where U_i and U_k are the voltage to ground (V) from electrodes i and k, respectively.

Considering that $P_{u,\ ik}$ is dissipated in an equal form from both electrodes, the effective power dissipated $P_{u,\ i}$ and $P_{u,\ k}$, from this only combination between the electrodes i and k, respectively, are:

$$P_{u,\ i} = P_{u,\ k} = \frac{P_{u,\ ik}}{2} \tag{3.18}$$

To be able to estimate $P_{u,\ Ei}$, the total effective power dissipated from electrode i is the sum of the effective power dissipated from all combinations possible for this electrode in question. The number of possible combinations n_e for each electrode is 10.

$$P_{u,\ Ei} = \frac{1}{2} \sum_{k=1}^{n_e} P_{u,\ ik} \tag{3.19}$$

Once this value is obtained, it calculates the power introduced $P_{u,\ phase}$ from each phase (R, S and T), by taking into consideration all four electrodes from this specific phase. In the following calculations, the n_e number of significant terms for the sum.

$$P_{u,\ phase} = \sum_{i=1}^{n_e} P_{u,\ Ei} \tag{3.20}$$

To calculate the total power inserted in the glass $P_{u,RST}$, a sum is made with all the $P_{u,phase}$:

$$P_{u,\ RST} = \sum_{i=1}^{n_e} P_{u,\ phase} \tag{3.21}$$

To be able to calculate the efficiency of the conversion from electric to thermal energy, it is necessary to determine the total power provided by a phase from an Alternating-Current (AC) circuit, denominated as theoretical power — $P_{t,\ phase}$, given in kW, and defined by:

$$P_{t,\ phase} = I_{phase} U_{phase} \tag{3.22}$$

where U_{phase} is the phase voltage (V) and I_{phase} represents the phase electric current (A).

The total theoretical power $P_{t,RST}$ provided by the transformer can be represented by the sum of the theoretical power supplied from each phase:

$$P_{t,\ RST} = \sum_{i=1}^{n_e} P_{t,\ phase} \tag{3.23}$$

After all, the efficiency of the conversion is performed, for the phase power and for the total power:

$$\eta_{phase} = \frac{P_{u,phase}}{P_{t,phase}} \tag{3.24}$$

$$\eta_{RST} = \frac{P_{u,RST}}{P_{t,RST}} \tag{3.25}$$

Furthermore, an extra calculation is performed to ensure that the electrode is not suffering an accelerated erosion from a current higher than it can support. Gruenberg [30] affirms that for furnace design purposes, 1.550 $\mathrm{A} \cdot \mathrm{cm}^{-2}$ is often used as a safe maximum. To determine the current density $I_{d,\ Ei}$ on the electrode i, it is necessary to take into account the surface area of the electrode and its electric current I_{Ei}.

$$I_{d,\ Ei} = \frac{I_{Ei}}{2\pi \frac{d}{2} l + \pi \left(\frac{d}{2}\right)^2} \tag{3.26}$$

Although the electrode can be used at the design maximum, it considers an equal current distribution on the electrode surface. which is not observed in the real operation. Considering a pencil effect on the electrode, caused by the greater current density at the front edge of the electrode, Gruenberg [30] assumed that 0.3048 m was affected by this effect. Then, recalculating this new surface area, it is possible to obtain the electrode current density $I_{d-c,\ Ei}$, considering the mentioned wear.

$$I_{d-c,\,Ei} = \frac{I_{Ei}}{2\pi\frac{d}{2}(l-0.3048)+\pi\frac{d}{2}\sqrt{\frac{d}{2}^2+0.3048^2}} \tag{3.27}$$

3.2.3 Power Dissipation Calculation

The power dissipated in the melt can be generated by the glass resistance and by the electrode resistance. Considering that there was a perfect distribution of the electric field around the electrode, and if the power dissipated from the electrode resistance can be disregarded, Gruenberg [30] developed Equation 3.30 that expresses a perfect imaginary cylinder of radius X (m) around the electrode where all the total effective power $P_{u,\,Ei}$, from this electrode, is dissipated uniformly.

To determine if the electrode resistance can be disregarded or not, it is considered insignificant if the power generated by the electrode resistance is less than 1 % of the power generated by the melt resistance. To calculate the electrode resistance R_e (Ω), it is taken into consideration the electrode cross-sectional area, length, and electric current. It is important to mention that since there is only information about the electrode's electric current, the power calculation will be given by square current and resistance.

$$R_e = \rho_e \frac{L}{A} \tag{3.28}$$

$$P_{R,\,Ei} = I_{Ei}^2 R_e \tag{3.29}$$

Once both values of $P_{u,\,Ei}$ and $P_{R,\,Ei}$ — power generated by the electrode resistance (kW) — are calculated, it is possible to determine if the electrode resistance will be taken into account or not, depending on its significance. In case it is accountable, the power generated by the electrode resistance will be added to the $P_{u,\,Ei}$.

The representation of the mentioned cylinder is shown in Figure 3.2. It is important to mention that, in this equation, $P_{u,\,Ei}$ is used in W. The equation developed by Gruenberg, referred above, is:

$$P_{u,\,Ei} = \frac{I_{E_i}^2\,\rho}{2\pi l}\int_{\frac{d}{2}}^{X}\frac{1}{X}\,dx \tag{3.30}$$

Then, by isolating the variable X, it is possible to obtain:

$$X = \exp\left(\frac{P_{u,\,Ei}\,2\pi l}{I_{E_i}^2\rho} + \ln\frac{d}{2}\right) \tag{3.31}$$

From the Equations 3.30 and 3.31, it is assumed that the greater the radius X, the more uniform the power distribution. It is important to mention that the top surface of the electrode is disregarded in calculating this volume, since usually, electrode rods are long and thin ($l >> d$).

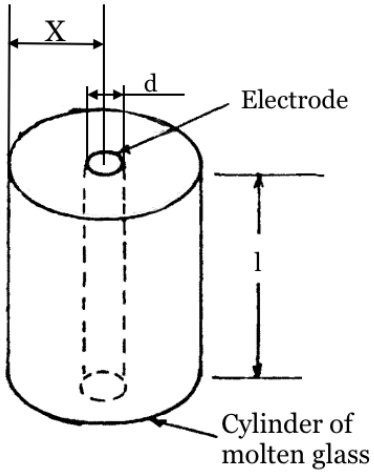


Figure 3.2: Representation of the perfect imaginary cylinder of molten glass, adapted [30].

To determine a limit for the term X, a maximum equivalent radius X_{eq} (m) was defined, which represents the radius of a cylinder that has the total glass melt volume V_{gm} (m^3). Then, if X exceeds X_{eq}, X_{eq} takes precedence over X in consideration. The term V_{gm} is calculated based on the dimensions of the melting tank (length, width, and effective glass height) subtracted by the volume of the electrodes within the tank, as in Equation 3.32. The calculation of X_{eq} is presented in Equation 3.33.

$$V_{gm} = 16.002 \cdot 8.534 \cdot 1.448 - 12\pi l \left(\frac{d}{2}\right)^2 \tag{3.32}$$

$$X_{eq} = \sqrt{\frac{V_{gm} + \pi l \left(\frac{d}{2}\right)^2}{\pi l}} \tag{3.33}$$

3.2.4 Heat Transfer Calculation

For the heat transfer calculation, once each electrode has its own imaginary glass cylinder around itself, and the cylinder's radius is estimated, it is possible to calculate the volume that is being affected by the temperature rise. For the electrodes that reached the maximum equivalent radius, the volume under its influence is V_{gm}, as expected. The glass cylinder volume for each electrode is performed by calculating its volume and subtracting the volume of the electrode:

$$V_i = \pi l X_i^2 - \pi l \left(\frac{d}{2}\right)^2 \tag{3.34}$$

where V_i is the volume (m^3) and X_i is the radius of the imaginary glass cylinder for the i^{th} electrode.

Once the volume is calculated, by using the glass density γ (kg m^{-3}), it is possible to

calculate the mass of the imaginary cylinder m_i (kg).

$$m_i = V_i\,\gamma \tag{3.35}$$

Through the heat transfer principles [42], displayed in Equation 3.36, it is possible to determine the temperature increase rate on the imaginary cylinder around each electrode, presented in Equation 3.37. Subsequently, it is calculated the temperature increase after a time t (s), as shown in Equation 3.38.

$$P_{u,\,Ei} = \frac{m_i\,c_p\,(T_f - T_i)}{t} \tag{3.36}$$

$$\frac{T_f - T_i}{t} = \frac{P_{u,Ei}}{m_i c_P} \tag{3.37}$$

$$T_f = \frac{P_{u,Ei}}{m_i c_P} t + T_i \tag{3.38}$$

where T_f is the final temperature (°C), T_i is the initial temperature (°C), c_p is the specific heat of the glass melt at constant pressure $\left(\text{kJ kg}^{-1}\,{}^{\circ}\text{C}^{-1}\right)$, and m is the mass of the imaginary cylinder around the electrode (kg).

3.2.5 Sensitivity Analysis

To assess the influence of measurement errors on the operational data obtained, the phases and system efficiencies were calculated with a 5 % variation in the operational parameters. Despite some rounding errors, the measurement error is more relevant and likely, as high-accuracy equipment is not typically required in this industry compared to laboratory studies.

The error was applied to the voltage to ground for each terminal ($V_{terminal}$), the voltage of each phase (V_{phase}), and the electric current of each phase (I_{phase}). The calculations, as presented earlier in this chapter (Equation 3.17 to 3.25), were performed accordingly. Finally, the lower and higher limits were obtained, representing the two extremes: a lower voltage gradient with a lower current and a higher voltage gradient with a higher current, respectively.

Chapter 4

Results and Discussion

The Results and Discussion section of this master thesis will present the findings obtained through implementing the methodology outlined earlier. This chapter will follow the same order as the Methodology chapter, providing a clear and logical flow of information. The results will be presented systematically, highlighting the key findings and observations. Additionally, a discussion will be provided, delving into the implications, limitations, and significance of the results obtained. Through an analysis of the data, this discussion aims to provide a deeper understanding of the research questions.

4.1 Electrical Resistivity

For the recipe composition presented in Chapter 3, calculations were performed to obtain the VFT equation for both models. Mazurin model obtained values for T_o of 799.7, B of 201.7, and C of 0.5005. The equation obtained is presented below, being the electrical resistivity given in Ω cm.

$$\log_{10}\rho = 0.5005 + \frac{201.7}{(T - 799.7)} \tag{4.1}$$

Fluegel model obtained values for T_o of 171.3, B of 1865, and C of -0.8725. The electrical resistivity is also given in Ω cm.

$$\log_{10}\rho = -0.8725 + \frac{1865}{(T - 171.3)} \tag{4.2}$$

The graphs from Figures 4.1 and 4.2 were created using a temperature step of 1 ºC from the mentioned models. As mentioned in Chapter 3, the Mazurin model is developed for temperatures between 600 ºC and 1400 ºC, while the Fluegel model is for temperatures between 1000 ºC and 1400 ºC. To facilitate the comparison between both models, temperatures below 1000 ºC were not included in the graph for the Mazurin model, since it has no relevance to this study.

Figure 4.1 illustrates the logarithmic function depicting the relationship between glass melt electrical resistivity and temperature. Figure 4.2 displays the function showcasing the correlation between glass melt electrical resistivity and temperature.

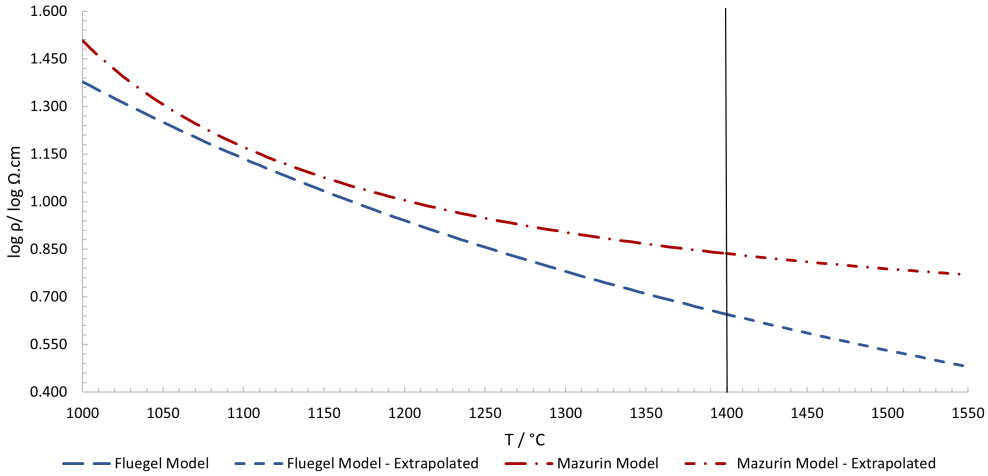


Figure 4.1: Representation of the logarithmic function of the glass melt electrical resistivity, for Mazurin and Fluegel models, and their extrapolation from 1400 to 1550 ºC.

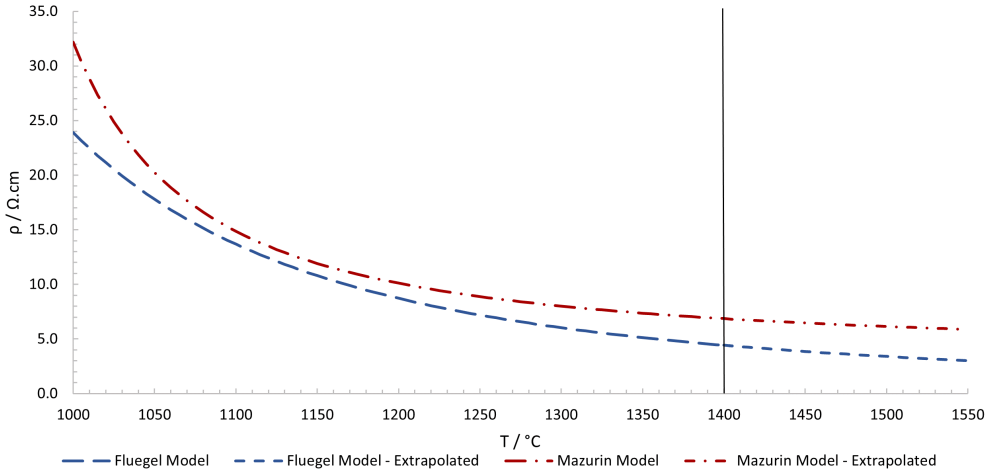


Figure 4.2: Representation of the function of the glass melt electrical resistivity, for Mazurin and Fluegel models, and their extrapolation from 1400 to 1550 ºC.

Table 4.1 presents the electrical resistance calculated from both models for the temperatures of 1400 ºC, 1450 ºC and 1550 ºC. The first line of data represents the upper limit temperature for both models, the second line is the temperature used for further comparison with other studies, and the third line is the considered glass melt temperature.

Table 4.1: Electrical resistivity values obtained from the two models

Temperature	**Mazurin Model — ρ (Ω.cm)**	**Fluegel Model — ρ (Ω.cm)**
1400 °C	6.863	4.422
1450 °C	6.466	3.857
1550 °C	5.879	3.023

As Figure 4.2 shows, both extrapolated curves present a trend to converge into the same range of values. Both models can be validated by a study developed by Varshneya, in which high-temperature electrical resistivity was measured for different types of container glasses [37].

In this study, a resistivity range from 3 to 8 Ω cm was obtained at 1450 ºC, also it was noticed an increase in the values when decreasing temperatures, e.g. 11 to 45 Ω cm at 1000 ºC. It was also found a convergence trend on this parameter. As presented in Table 4.1, at 1450 ºC, the values obtained from both models fit the range presented by Varshneya, at the same temperature. The same happens to the values at 1000 ºC.

Although both models are developed for temperatures below 1400 ºC, both models were extrapolated since no other model was found in the literature. Furthermore, taking into consideration the convergence of the values obtained and its similarity to the experimental values, presented above, both models can be considered as a good fit to reality. Due to the model's complexity, the Fluegel third-order model was considered more reliable since it takes into account binary and ternary glass forming systems (namely $Na_2O - K_2O - CaO$), while the second-order model developed by Mazurin considers just a few binary systems.

4.2 Electrical Resistance

Initially, it was calculated the resistance from each pair of electrodes from different terminals. Then, its effective power dissipated is calculated considering the voltage differential from the combination of electrodes. As stated in Chapter 3, it is essential to reiterate that the measurement equipment used for electric current, both for the phases I_{phase} and the electrodes I_{E_i}, as well as for the voltage to ground of each terminal (e.g., U_{R1}), possesses an unknown level of precision. Furthermore, it should be noted that the data provided by the software is presented solely as rounded numbers without any decimal places. The values obtained for the resistance R_{ik} and effective power dissipated $P_{u,\,ik}$ for each pair are presented in the Tables C.1 and C.2, on Appendix C.

The provided tables reveal a limited range of values for the resistance R_{ik} between electrodes from different terminals. As resistance depends solely on the layout and dimensions of the electrodes and furnace, it remains constant across various scenarios. Notably, the pairs E12-E5 and E9-E4 exhibit the highest resistance values — 0.0967 Ω, while the pairs E2-E3 and E7-E6 demonstrate the lowest resistance values — 0.0608 Ω. It is evident that there is a proportional relationship between distance and resistance: the farther apart the electrodes, the higher the resistance, and conversely, the closer the electrodes, the lower the resistance.

In terms of the effective power dissipated by each electrode pair, a notable observation is that electrodes from terminal T2 have a significant influence due to their high voltage to ground value. It is worth mentioning that, in Table C.1, the values for the R1-S1 terminal pair in scenario 4 are recorded as null. This is because there is no potential gradient between the terminals in this specific scenario. Additionally, electrode pairs connected to terminals with similar voltage to ground values demonstrate minimal impact on power dissipation. Subsequently, the total effective power dissipated $P_{u,\ Ei}$ by each individual electrode was estimated, considering all possible combinations. These values for each electrode can be found in Table 4.2.

Table 4.2: Effective power dissipated from each electrode

Phase	**Terminal**	**Electrode**	$P_{u,Ei}$ (kW)			
			Scenario 1	Scenario 2	Scenario 3	Scenario 4
R	R1	E1	95.4	96.9	82.4	94.5
		E2	95.8	97.8	82.7	95.1
	R2	E9	223	202	196	169
		E10	224	203	196	169
S	S1	E7	131	126	121	127
		E8	121	116	111	115
	S2	E11	95.4	90.0	81.2	81.5
		E12	93.3	89.0	80.2	80.6
T	T1	E3	91.6	89.3	79.8	84.6
		E4	91.1	88.5	79.5	84.4
	T2	E5	457	447	420	465
		E6	471	462	433	480

As shown in Table 4.2, the electrodes with a more significant difference in voltage to ground values, namely E9 and E10 from terminal R2, and mainly E5 and E6 from terminal T2, exhibit higher effective power dissipation, confirming the affirmation mentioned above. This phenomenon can be attributed to the magnitude of the potential gradient generated by these electrodes with the remaining pairs.

As anticipated, the magnitudes of the values remained consistent across different scenarios. The most significant change was observed in electrodes E9 and E10, which both experienced a reduction in their effective power dissipated by 24.4 % when comparing the scenarios with the greatest disparities. This outcome can be attributed to the increase in their voltage to ground values, consequently decreasing the voltage gradient when compared with the remaining terminals.

Subsequently, to provide a clearer representation of the findings, the effective power $P_{u,\ phase}$, the theoretical power $P_{t,\ phase}$, and their corresponding efficiencies η_{phase}, were estimated for each individual phase as well as for all phases collectively, indicated as $P_{u,\ RST}$, $P_{t,\ RST}$, and η_{RST}, respectively. Based on these calculations, Table 4.3 was constructed to present the derived values for the theoretical power, effective power, and efficiency of each phase as well as the combined phases.

Table 4.3: Calculated operational parameters

Phase	Parameter	Scenario 1	Scenario 2	Scenario 3	Scenario 4	Units
R	$P_{t,\,R}$	329	310	336	354.4	kW
	$P_{u,\,R}$	310	299	277	264	kW
	η_R	94.1%	96.4%	82.3%	74.4%	
S	$P_{t,\,S}$	338	313	337	355	kW
	$P_{u,\,S}$	211	210	195	202	kW
	η_S	62.5%	67.0%	57.8%	56.9%	
T	$P_{t,\,T}$	912	904	872	904	kW
	$P_{u,\,T}$	546	542	504	557	kW
	η_T	59.9%	60.0%	57.8%	61.7%	
All Phases	$P_{t,\,RST}$	1579	1527	1546	1614	kW
	$P_{u,\,RST}$	1067	1051	975.5	1023	kW
	η_{RST}	67.6%	68.8%	63.1%	63.4%	

Table 4.3 shows that the theoretical power supplied to each phase and the entire system remains relatively consistent across different scenarios. However, the effective power varies, leading to different efficiencies for both the phases and the system. Notably, phase R demonstrates the highest efficiency in converting electricity to thermal energy, reaching its peak at 96.4 % in scenario 2 and dropping to its lowest at 74.4 % in scenario 4. Phases S and T exhibit similar efficiency levels, with phase S achieving an efficiency of 67.0 % in scenario 2. Overall, the electrical boosting system demonstrates an efficiency ranging from 63.1 % to 68.8 % across the four scenarios.

In the glass industry, the system is expected to achieve an efficiency ranging from 80 % to 90 % (information provided by supplier companies). Staněk affirms that the transfer of electrical to thermal energy through electric current is very high, ranging around 90 % or even higher [21]. The main sources of anticipated losses in this system are resistive losses and radiative losses. Resistive losses occur due to the resistance encountered by conductors in the circuit, leading to energy being dissipated by Joule heating. In the electrical boosting system, minimising losses in conductors such as wires and busbars is crucial, while maximising losses in the glass melt. This emphasis is placed on converting electrical energy into thermal energy to effectively heat the glass melt. Radiative losses, on the other hand, result from the electromagnetic field generated by current flow in the conductor. Some of the energy from this field is emitted as electromagnetic waves, causing heating effects on surrounding materials, particularly those with higher electrical conductivity.

The transformer is responsible for transforming and supplying the power to the electrical boosting system, through different voltage phases. As most electrical equipment, the transformer can experience energy losses that are influenced by its characteristics and time in service. These losses tend to increase over time, resulting in decreased efficiency. It is common practice to reuse transformers from dismantled furnaces or other sources. Additionally, eddy current and hysteresis losses can occur in the transformer's core due to the alternating current nature and variations in the magnetic field [43].

To achieve more accurate and reliable results, it is evident that the development of more sophisticated modelling approaches is necessary. Curran [25] employed a computer program based on a lumped parameter network-type thermal analyser to determine heat generation through the Joule effect. This study utilised a multi-node model, considering a two-dimensional power density distribution. The results of this is study will be mentioned in Subsection 4.3. However, due to limited data availability, creating such a complex model would not be feasible. As mentioned earlier, the obtained values are not as precise as expected for this type of calculation since the voltage and electric current are derived from operating values through arithmetic calculations, instead of vectorial ones.

The absence of understanding about electrical boosting systems in the industry is also a very limiting factor. This can be observed when performing bibliographic research, where just a minimal amount of articles, books and studies from the last 60 years can be found. The most relevant authors, such as Staněk [21, 29, 40], Curran [25] and Gruenberg [30], have their main publications on the topic in the seventies and eighties. No recent and relevant knowledge about the electrical boosting design and operation is found in the public or under the publishing companies' domain.

Another significant consideration pertains to the ohmic property. Although there is no explicit information available regarding whether glass exhibits ohmic characteristics, it could potentially explain why the observed values are lower than expected. Non-ohmic conductors do not conform to Ohm's law, which implies the absence of a linear relationship between applied voltage and current, resulting in varying resistance with changing the applied voltage. To ascertain whether a conductor is ohmic or not, it is necessary to subject the material to different voltage levels, measure the corresponding electric currents, and plot a graph with a regression analysis of the data. If the graph exhibits a straight line, indicating a constant resistance, the material can be deemed ohmic.

Subsequently, an additional critical analysis entails comparing the current density values of each electrode against their designated maximum safe limit. This comparative examination serves as a crucial assessment to ensure that the current density remains within the permissible range for each electrode, thereby guaranteeing safe operational conditions. According to Gruenberg [30], the maximum safe limit used by many furnace designers is 1.550 $A \cdot cm^{-2}$. The current density values for each electrode in their initial conditions, disregarding any wear from erosion, are presented in Table 4.4.

Table 4.4: Current density on each electrode, disregarding any wear from erosion

Phase	**Electrode**	$I_{d,\,Ei}$ ($\mathrm{A \cdot cm^{-2}}$)			
		Scenario 1	Scenario 2	Scenario 3	Scenario 4
R	E1	0.7380	0.7689	0.7274	0.7412
	E2	0.9536	0.9878	0.9430	0.9560
	E9	0.7648	0.8136	0.7689	0.7803
	E10	0.9227	0.9389	0.8950	0.9129
S	E7	0.8063	0.8291	0.7852	0.8006
	E8	0.7575	0.7632	0.7258	0.7518
	E11	0.8250	0.8421	0.7909	0.8250
	E12	0.6989	0.7079	0.6745	0.6851
T	E3	1.513	1.518	1.524	1.484
	E4	1.465	1.433	1.462	1.410
	E5	1.510	1.488	1.518	1.444
	E6	1.471	1.466	1.471	1.454

As can be observed, all of the electrodes respect the maximum safe limit mentioned above. The electrodes from phase T, namely E3, E4, E5 and E6 are nearly close to the limit since they have high electric current, operating under safe conditions. However, since these calculations were made from the initial conditions of the electrode, disregarding the wear caused by erosion during its operation, a new calculation can be performed, taking them into account. The main cause of this wear is the high current density in the front edge of the electrode. The current density value for each electrode, considering the mentioned operation wear, is presented in Table 4.5.

Table 4.5: Current density on each electrode, considering wear from erosion

Phase	**Electrode**	$I_{d-c,\,Ei}$ ($\mathrm{A \cdot cm^{-2}}$)			
		Scenario 1	Scenario 2	Scenario 3	Scenario 4
R	E1	1.039	1.082	1.024	1.043
	E2	1.342	1.390	1.327	1.345
	E9	1.076	1.145	1.082	1.098
	E10	1.298	1.321	1.260	1.285
S	E7	1.135	1.167	1.105	1.127
	E8	1.066	1.074	1.021	1.058
	E11	1.161	1.185	1.113	1.161
	E12	0.9836	0.9962	0.9492	0.9641
T	E3	2.129	2.137	2.145	2.088
	E4	2.062	2.016	2.058	1.984
	E5	2.125	2.094	2.137	2.032
	E6	2.070	2.063	2.070	2.046

Upon careful evaluation of the wear during continuous operation, it is evident that all electrodes from phase T exceed substantially the maximum safe limit set in each scenario. This indicates that the phase T electrodes were inadequately designed without considering the wear from erosion. Consequently, it is crucial to prioritise frequent and regular maintenance for these

electrodes. A common industry practice for maintenance involves pushing the electrode inwards and rotating them 90º to keep the current density below the specified safe maximum. During furnace planning, it is necessary to account for this requirement by estimating longer electrodes that will periodically require pushing into the furnace.

Despite not being accounted for in the calculations, it is essential to acknowledge that corrosion is another significant factor directly impacting the electrodes. Factors such as the electrode's loading by alternating current and the presence of substances capable of oxidising the electrode material (e.g., lead oxide, refining and colouring agents) play a pivotal role in corrosion. It is worth noting that in the majority of furnaces employing electrical boosting, the electrodes are composed of molybdenum, a costly material that, when corroded, can adversely affect the colour of the glass [21]. Given these circumstances, it is crucial to minimise the corrosion of the electrodes to ensure optimal performance and maintain the desired glass colour.

4.3 Power Dissipation

Another source of power generation comes from the electrode resistance. Molybdenum electrodes are good conductors, then, should not generate much power from their resistance. From calculating the electrode resistance for all 12 electrodes for each scenario, it is possible to confirm that none achieves a level of 0.50 % or above of the calculated effective power from each electrode, presented earlier.. Thus, the power dissipated by the resistance of the electrode is negligible. The values for the power generated from the electrode resistance can be found in Table 4.6.

Table 4.6: Power generated from the electrode resistance

Phase	**Electrode**	$P_{R,\,Ei}$ (kW)			
		Scenario 1	Scenario 2	Scenario 3	Scenario 4
R	E1	0.0376	0.0408	0.0365	0.0379
	E2	0.0628	0.0674	0.0614	0.0631
	E9	0.0404	0.0457	0.0408	0.0420
	E10	0.0588	0.0608	0.0553	0.0575
S	E7	0.0449	0.0475	0.0426	0.0443
	E8	0.0396	0.0402	0.0364	0.0390
	E11	0.0470	0.0490	0.0432	0.0470
	E12	0.0337	0.0346	0.0314	0.0324
T	E3	0.189	0.190	0.192	0.182
	E4	0.177	0.170	0.176	0.164
	E5	0.188	0.183	0.190	0.172
	E6	0.179	0.178	0.179	0.174

These values obtained were inside the expected range. As mentioned above, molybdenum electrodes present an extremely low resistivity under the operation conditions, in the same order of magnitude as copper and iron under normal conditions, being classified as a good electrical conductor. Thus, it is expected to not generate considerable losses from the electric current flow. The

highest values obtained in Table 4.6 can be justified by the high electric current that passes through the electrodes from phase T. Considering the effective power dissipated by each electrode, it can be affirmed that the electrodes E3 and E4 hold the highest significance, with the power dissipated from their electrode resistance reaching up to 0.24 % of the previously calculated effective power dissipation. However, it is evident that their influence is minimal.

Following this, considering that the power generated from the electrode resistance is insignificant, the radius X of a perfect imaginary cylinder surrounding the electrode was calculated, using the effective power dissipated presented in Table 4.2. This radius represents the volume within which the effective power dissipated from the melt resistance would be distributed if there were a perfectly uniform electric field surrounding the electrode [30]. In advance, the maximum equivalent radius X_{eq} for this furnace was determined to be 10.2 m. Any calculated radius exceeding this value will be considered as X_{eq}. The calculated values of the cylinder radius X for each electrode are presented in Table 4.7.

Table 4.7: Radius X of the perfect imaginary cylinder around the electrode

Phase	**Electrode**	X (m)			
		Scenario 1	Scenario 2	Scenario 3	Scenario 4
R	E1	10.2	10.2	10.2	10.2
	E2	10.2	10.2	10.2	10.2
	E9	10.2	10.2	10.2	10.2
	E10	10.2	10.2	10.2	10.2
S	E7	10.2	10.2	10.2	10.2
	E8	10.2	10.2	10.2	10.2
	E11	10.2	10.2	10.2	10.2
	E12	10.2	10.2	10.2	10.2
T	E3	0.846	0.763	0.531	0.742
	E4	1.03	1.09	0.671	1.03
	E5	10.2	10.2	10.2	10.2
	E6	10.2	10.2	10.2	10.2

In most scenarios, the calculated radius values correspond to the maximum equivalent radius of 10.2 m, indicating that the electrodes heat up the entire volume of the glass melt. However, electrodes E3 and E4 have a more limited influence, affecting a smaller volume surrounding them. While the other electrodes distribute their heating effect throughout the entire furnace volume, electrodes E3 and E4 primarily impact a localised volume around themselves. These outcomes can be explained by referring to Equation 4.3, wherein the most influential parameters are the introduced effective power $P_{u,\,Ei}$ (given in W) and the electric current I_{Ei} (A) associated with the i^{th} electrode. These two variables are the only ones that vary across different electrodes and scenarios, hence accounting for the observed differences in the radius of influence.

$$X = \exp\left(\frac{P_{u,Ei}}{I_{Ei}^2}\frac{2\pi l}{\rho} + \ln\frac{d}{2}\right) \tag{4.3}$$

Given this observation, a more comprehensive analysis is warranted to gain a better understanding of the obtained results. It is known that the term $\frac{2\pi l}{\rho}$ remains constant across all electrodes, as they share the same length l (m) and the glass melt exhibits a consistent electrical resistivity ρ (Ω m), resulting in a value of 124.8 Ω^{-1}. Similarly, the term $\ln\left(\frac{d}{2}\right)$ maintains a constant value of -1.204 since the diameter d of the electrodes remains consistent for all cases.

$$X = \exp\left(\frac{P_{u,Ei}}{I_{Ei}^2}124.8 - 1.204\right) \tag{4.4}$$

In this case, it is evident that the parameter X is dependent on the term $\frac{P_{u,Ei}}{I_{Ei}^2}$. For electrodes E3 and E4, this term ranges between 0.0228 Ω and 0.0285 Ω, depending on the scenario. However, for the remaining electrodes, this term varies from 2.5 to 9.5 times higher than the smallest values observed for electrodes E3 and E4. Figure 4.3 illustrates the relationship between the perfect imaginary cylinder radius and the ratio of effective power to the square of the current. It is noteworthy that a threshold of 10.2 m for the radius is reached after attaining a value of 0.0465 Ω for this ratio. This threshold corresponds to the equivalent radius.

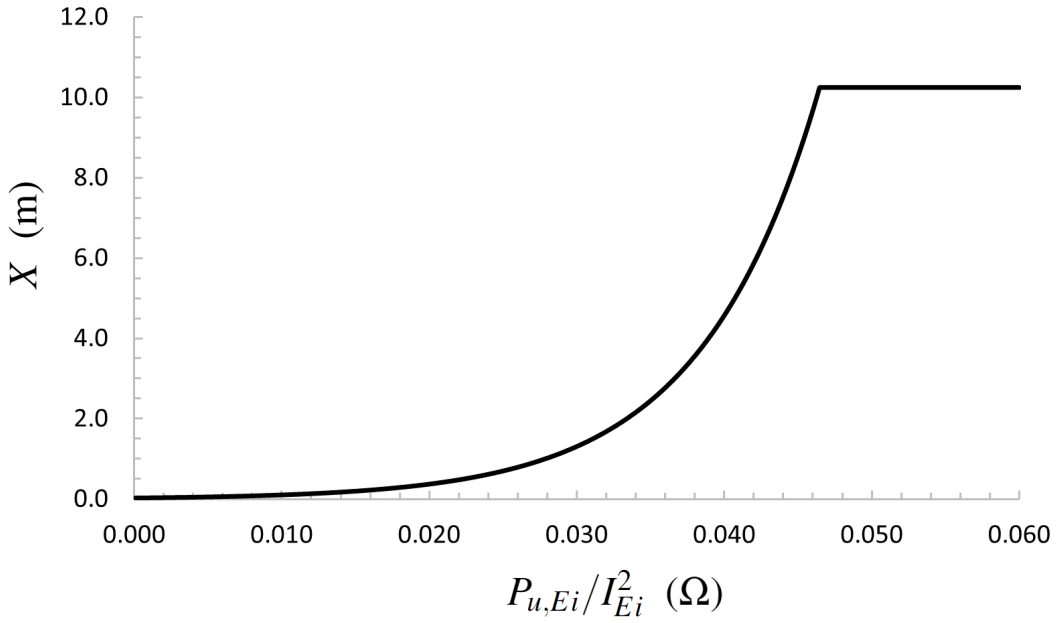


Figure 4.3: Dependence of the effective power ($P_{u,\,Ei}$) and square current (I_{Ei}^2) ratio on the imaginary cylinder radius (X).

The ratio presented in Figure 4.3 provides valuable insights into the relationship between current density and power dissipation. When considering a constant power dissipated, as the current density decreases, the energy dissipated in the vicinity of the electrode also decreases, assuming the electrode surface area remains constant. This observation aligns with the well-established

understanding that higher current densities result in a more concentrated power dissipation near the electrode surface. It should be emphasised that the impact of a change in the electric current I_{Ei} is greater than a change in the effective power $P_{u,\,Ei}$, since I_{Ei} is squared.

It is worth noting that most of the results obtained from Table 4.7 do not align with the findings of Gruenberg's study [30], which indicated that a significant portion of power dissipation occurs within a small fraction of the glass melting tank area. This discrepancy can be attributed to differences in effective power and square current ratio, besides the different conditions in both studies. Moreover, Curran [25] developed a study using a two-dimensional computer model which results showed that the power density at the surface of the electrode is around 20 times higher than a short distance from the electrode, where it gets uniform and stable. Comparing these results, it is clear that similarity is not found. Again, it can be attributed to differences in operation, since the temperature and glass properties are not the same.

In scenarios characterised by high current and low effective power, the ratio $\frac{P_{u,Ei}}{I_{Ei}^2}$ tends to be very small, leading to a shorter radius. This indicates that the power is primarily dissipated in the immediate vicinity of the electrode. The range for this ratio spans from the lower limit of 0 Ω to 0.0300 Ω. It must be highlighted that the value of 0 Ω corresponds to the radius of the electrode 0.031 m. Conversely, when the current is low and the effective power is high, a large radius is observed, signifying a more uniform power dissipation throughout the bulk of the melt. The corresponding values range from 0.0465 Ω and above, surpassing the defined threshold.

For cases where both the current and effective power is proportionally low or high, falling within the range of 0.0300 Ω to 0.0465 Ω, an intermediate radius is observed. This indicates that the power is partially dissipated within the bulk of the melt, striking a balance between local and distributed dissipation. It is crucial to note that the range presented for each condition is specific to the parameters and characteristics considered in this study. The terms in Equation 4.4 incorporate the dimensions and properties of the actual furnace analysed in this study. Therefore, the obtained range is applicable only within the context of this particular study and may not directly translate to other furnace configurations or operating conditions.

4.4 Heat Transfer

Considering the radius X calculated for each electrode from each scenario studied, it is calculated the volume of this perfect imaginary cylinder of glass melt. This volume disregards the volume occupied by the electrode. The volumes, in cubic meters, are presented in Table 4.8.

The obtained results support the conclusion that, except for E3 and E4, all electrodes contribute to the heating effect across the entire volume of the glass melt. This finding suggests a consistent and uniform distribution of power dissipation, which challenges theories proposing a limited distance of influence for power dissipation from the electrodes.

Subsequently, the rate of temperature increase within the volume influenced by the electrodes is calculated. This rate is measured in Celsius degrees per second. The values are presented in Table 4.9.

Table 4.8: The calculated volume of the perfect imaginary cylinder around the electrode

Phase	**Electrode**	$V(m^3)$			
		Scenario 1	Scenario 2	Scenario 3	Scenario 4
R	E1	198	198	198	198
	E2	198	198	198	198
	E9	198	198	198	198
	E10	198	198	198	198
S	E7	198	198	198	198
	E8	198	198	198	198
	E11	198	198	198	198
	E12	198	198	198	198
T	E3	1.35	1.10	0.529	1.04
	E4	2.01	2.24	0.847	2.01
	E5	198	198	198	198
	E6	198	198	198	198

Table 4.9: Temperature increase rate on the perfect imaginary cylinder around the electrode

Phase	**Electrode**	**Temperature Increase Rate** ($^{\circ}$C s^{-1})			
		Scenario 1	Scenario 2	Scenario 3	Scenario 4
R	E1	$1.45{\cdot}10^{-4}$	$1.47{\cdot}10^{-4}$	$1.25{\cdot}10^{-4}$	$1.44{\cdot}10^{-4}$
	E2	$1.46{\cdot}10^{-4}$	$1.49{\cdot}10^{-4}$	$1.26{\cdot}10^{-4}$	$1.44{\cdot}10^{-4}$
	E9	$3.39{\cdot}10^{-4}$	$3.08{\cdot}10^{-4}$	$2.98{\cdot}10^{-4}$	$2.56{\cdot}10^{-4}$
	E10	$3.40{\cdot}10^{-4}$	$3.09{\cdot}10^{-4}$	$2.99{\cdot}10^{-4}$	$2.57{\cdot}10^{-4}$
S	E7	$1.99{\cdot}10^{-4}$	$1.92{\cdot}10^{-4}$	$1.84{\cdot}10^{-4}$	$1.93{\cdot}10^{-4}$
	E8	$1.83{\cdot}10^{-4}$	$1.76{\cdot}10^{-4}$	$1.69{\cdot}10^{-4}$	$1.76{\cdot}10^{-4}$
	E11	$1.45{\cdot}10^{-4}$	$1.37{\cdot}10^{-4}$	$1.24{\cdot}10^{-4}$	$1.24{\cdot}10^{-4}$
	E12	$1.44{\cdot}10^{-4}$	$1.35{\cdot}10^{-4}$	$1.22{\cdot}10^{-4}$	$1.23{\cdot}10^{-4}$
T	E3	$2.04{\cdot}10^{-2}$	$2.46{\cdot}10^{-2}$	$4.54{\cdot}10^{-2}$	$2.46{\cdot}10^{-2}$
	E4	$1.36{\cdot}10^{-2}$	$1.18{\cdot}10^{-2}$	$2.82{\cdot}10^{-2}$	$1.26{\cdot}10^{-2}$
	E5	$6.95{\cdot}10^{-4}$	$6.80{\cdot}10^{-4}$	$6.38{\cdot}10^{-4}$	$7.08{\cdot}10^{-4}$
	E6	$7.17{\cdot}10^{-4}$	$7.02{\cdot}10^{-4}$	$6.59{\cdot}10^{-4}$	$7.30{\cdot}10^{-4}$

Assuming homogeneity and uniform temperature of the glass melt, it is possible to conclude that the total power introduced into the entire volume is the summation of power contributions from all electrodes, excluding E3 and E4. By considering the electrodes that influence the entire glass melt volume and summing their respective temperature increases over time, it is possible to evaluate the temperature increase after 1 hour of operation. The calculated values are as follows:

- In scenario 1, the glass melt temperature increases by $3.05 \cdot 10^{-3}$ $^{\circ}$C s^{-1}, and after 1 hour of operation, increases by 11.0 ºC.
- In scenario 2, the glass melt temperature increases by $2.94 \cdot 10^{-3}$ $^{\circ}$C s^{-1}, and after 1 hour of operation, increases by 10.6 ºC.

- In scenario 3, the glass melt temperature increases by $2.74 \cdot 10^{-3}$ °C s^{-1}, and after 1 hour of operation, increases by 9.88 ºC.
- In scenario 4, the glass melt temperature increases by $2.86 \cdot 10^{-3}$ °C s^{-1}, and after 1 hour of operation, increases by 10.3 ºC.

When analysing only electrodes E3 and E4, it is evident that their temperature increase rates are significantly higher compared to the remaining electrodes, which is expected given their significantly smaller influence volume. There is a slight variation observed among different scenarios, attributed to the radius of influence and corresponding volume changes. Examining their temperature increase after 1 hour of operation, a narrow range is observed:

- In scenario 1, the temperature increases by 73.5 ºC and 49.1 ºC after 1 hour of operation for electrodes E3 and E4, respectively.
- In scenario 2, the temperature increases by 88.4 ºC and 42.7 ºC after 1 hour of operation for electrodes E3 and E4, respectively.
- In scenario 3, the temperature increases by 163 ºC and 102 ºC after 1 hour of operation for electrodes E3 and E4, respectively.
- In scenario 4, the temperature increases by 88.5 ºC and 45.4 ºC after 1 hour of operation for electrodes E3 and E4, respectively.

Although the temperature increase rate can be calculated, it is important to note that further calculations cannot be performed due to the lack of information regarding the flow and dynamics of the glass melt. Despite the example of a 1-hour duration provided for the sake of clarity in understanding the temperature increase, it remains uncertain for how long the same glass particles will be heated up.

The obtained temperature increase values should be carefully analysed, as a high rate of temperature increase on a localised volume can lead to a quicker reduction in density, resulting in a separate glass bulk that does not mix with the rest of the glass due to density differences. With the rates exhibited by electrodes E3 and E4, within their small influence volume, they have the potential to disrupt the flow path of the glass, resulting in production defects due to inadequate residence time for meeting quality standards. If this situation continues over an extended period, the overheated glass bulk may ultimately lead to a critical furnace failure.

4.5 Sensibility Analysis

A sensibility analysis was performed taking into account a 5 % variation of the voltage to ground ($V_{terminal}$) and the phase current values (I_{phase}). Both parameters were selected for this analysis since are the ones that presents the lower reading sensitivity, besides having a poor rounding. The main focus of this analysis is to asses how phase and system efficiency behaves for each scenario when performing the mentioned variation. Must be mentioned that the theoretical power is also influenced. Tables 4.10 and 4.11 present the lower and higher limit for each scenario considering the variation, for scenarios 1 and 2, 3 and 4, respectively.

Table 4.10: Sensibility analysis on operational parameters for scenarios 1 and 2

		Scenario 1			Scenario 2		
Phase	Parameters	Lower Limit	Original	Higher Limit	Lower Limit	Standard	Higher Limit
R	$P_{t,\,R}$	296.8	328.8	362.5	280.1	310.4	342.2
	$P_{u,\,R}$	204.5	309.5	362.5	199.0	299.2	342.2
	η_R	68.9%	94.1%	100%	71.1%	96.4%	100%
S	$P_{t,\,S}$	305.1	338.1	372.8	282.2	312.7	344.7
	$P_{u,\,S}$	131.7	211.2	333.7	134.1	213.1	331.7
	η_S	43.2%	62.5%	89.5%	47.5%	68.2%	96.2%
T	$P_{t,\,T}$	823.1	912.0	1005	815.9	904.0	996.7
	$P_{u,\,T}$	351.6	546.0	797.1	350.4	546.0	795.2
	η_T	42.7%	59.9%	79.3%	42.9%	60.4%	79.8%
All Phases	$P_{t,\,RST}$	1425	1579	1741	1378	1527	1684
	$P_{u,\,RST}$	687.9	1067	1584	683.5	1058	1562
	η_{RST}	48.3%	67.6%	91.0%	49.6%	69.3%	92.8%

On Phase R, the sensibility analysis for the Higher Limit was calculated with a variation lower than 5 %, for both scenarios.

Table 4.11: Sensibility analysis on operational parameters for scenarios 3 and 4

		Scenario 3			Scenario 4		
Phase	Parameters	Lower Limit	Original	Higher Limit	Lower Limit	Standard	Higher Limit
R	$P_{t,\,R}$	303.5	336.3	370.8	319.9	354.4	390.7
	$P_{u,\,R}$	179.3	276.7	370.8	174.4	263.6	390.7
	η_R	59.1%	82.3%	100%	54.5%	74.4%	100%
S	$P_{t,\,S}$	304.0	336.9	371.4	320.7	355.3	391.7
	$P_{u,\,S}$	118.4	194.6	313.7	129.7	201.8	318.9
	η_S	38.9%	57.8%	84.5%	40.5%	56.8%	81.4%
T	$P_{t,\,T}$	787.3	872.3	961.7	815.6	903.8	996.4
	$P_{u,\,T}$	321.7	503.5	741.2	360.9	556.8	810.7
	η_T	40.9%	57.7%	77.1%	44.2%	61.6%	81.4%
All Phases	$P_{t,\,RST}$	1395	1546	1704	1456	1613	1779
	$P_{u,\,RST}$	619.3	975	1468	665.0	1022	1523
	η_{RST}	44.4%	63.1%	86.2%	45.7%	63.4%	85.6%

On Phase R, the sensibility analysis for the Higher Limit was calculated with a variation lower than 5 %, for both scenarios.

Upon analysing efficiency variations for different scenarios, it is evident that the system's upper limit falls within the expected range. Phase R consistently exhibited efficiency of 100 % across all scenarios, while performing a sensibility analysis with a variation lower than 5 %. This may be attributed to its lower voltage operation, more precise measurements due to potentially

better equipment conditions, which implies a lower error. It is essential to emphasise that the useful power is directly proportional to the square of the voltage gradient, while the theoretical power is only proportional to the phase voltage.

Phase S demonstrated efficiencies ranging from 81.4 % to 96.2 %, all of which fell within the expected range. Phase T, as expected for an electrical boosting system in operation, presented efficiencies around the minimum threshold of 80 %, reaching 81.4 % in scenario 4.

The overall system efficiency ranged from 85.6 % to 92.8 %, aligning well with both industry standards and the findings by Staněk [40]. As earlier discussed in this chapter, it can be affirmed that the imprecision of the measurement equipment can have influence on the calculated efficiency for each scenario. However, when evaluating the lower limit, the results were even lower than the original values, as it is anticipated.

Chapter 5

Conclusions

5.1 Achievements

The primary aim of this study was to develop a comprehensive mathematical model that accurately represents the power dissipation within an operational glass-melting furnace's electrical boosting system, specifically focusing on the power distribution and overall efficiency of the glass melt. Additionally, this research aimed to provide a deeper theoretical understanding of the electrical boosting operation.

The developed mathematical model takes into account various factors, including the temperature and chemical composition of the melted glass, the dimensions of the furnace and its electrical boosting system, and the operational parameters. Different scenarios were examined, considering identical chemical compositions but varying electric current and voltage. The chosen approach for the model was arithmetic.

To gather relevant knowledge and insights, a thorough review of academic publications and books was conducted. However, it became evident a notable dearth of information regarding electrical boosting design and operation. The most recent studies were dated back to the 1970s and 1980s. Among the most influential authors in this field were Staněk [21, 29, 40], Curran [25], and Gruenberg [30]. Their equations formed the foundation of the mathematical model developed in this study.

By considering the voltage gradient across each pair of electrodes, the effective power dissipation from every electrode was accurately calculated. As anticipated, electrodes exhibiting higher voltage gradients demonstrated greater effective power. To assess efficiency, a comparison was made between the effective power of each phase, based on the electrode power, and the theoretical power of each phase. The efficiency calculations yielded the following results for different scenarios: phase R ranged from 74 % to 94 %, phase S ranged from 57 % to 67 %, and phase T ranged from 57 % to 62 %. The overall efficiency of the electrical boosting system ranged from 63 % to 69 %. While it is expected for these systems to achieve an efficiency of 80 % or higher, several factors contribute to this disparity. Losses within the electrical plant, such as those occurring in wires, busbars, and transformers, can generate inefficiencies. Additionally, imprecise

measurements of electrical parameters can also impact the accuracy of the results. An assessment of the current density was also conducted. In all the different scenarios, the electrodes from phase T consistently exhibited values above the safe maximum limit, taking into account the wear incurred during operation. This indicates a potential issue with excessive current density, which could lead to accelerated electrode degradation.

The power dissipation analysis revealed a distinct relationship between effective power and square current ratio, and the radius of the imaginary cylinder surrounding the electrode. Varying this ratio led to different power dissipation profiles. Smaller ratios indicated a shorter radius of power dissipation around the electrode. However, as the ratio increased, the radius expanded exponentially, resulting in more intense power dissipation within the bulk of the glass melt. A threshold of 10.2 m was defined for the mentioned radius, representing the total volume of the glass melt.

Throughout the different scenarios, consistent behaviour was observed for each electrode. Notably, electrodes E3 and E4 from terminal T1 of phase T were the only ones that remained below the threshold, operating within a radius range of 0.53 to 1.1 m. When assessing heat transfer, it became evident that these two electrodes experienced a higher rate of temperature increase due to their smaller influence volume. For the mentioned electrodes, the temperature increase rate ranged from 0.012 ºC s^{-1} to 0.045 ºC s^{-1}. In contrast, the remaining electrodes exhibited temperature increase rates approximately 100 times lower in magnitude.

Given these findings, it is crucial to exercise caution during operation, as high-temperature increase rates in small volumes have the potential to disrupt the flow path of the glass, resulting in production defects. Therefore, meticulous attention should be paid to the operational aspects to ensure smooth and defect-free glass production.

5.2 Future Work

To enhance the mathematical model and achieve a more accurate simulation of the effective electrical boosting heating in the glass melting process, several key steps should be taken. Firstly, employing a computational fluid dynamics approach is essential to effectively model the dynamic glass flow inside the furnace. Additionally, a novel approach involving a vectorial calculation should be considered to address phase mismatch and improve accuracy. Furthermore, a more sophisticated computational modelling technique incorporating field lines and perpendicular equipotential lines would enable a comprehensive assessment of power dissipation gradients.

An additional avenue to explore is the development of a predictive tool that can determine the optimal timing for electrode maintenance. This tool could leverage erosion and corrosion predictions based on various operational conditions, including temperature, flow rate, chemical composition, and electric current for each electrode. Lastly, conducting a small-scale laboratory test on a glass melting tank with electrical boosting is recommended to measure the relationship between voltage and electric current. This experiment would provide valuable insights into confirming the ohmic properties across different types of glass melts.

Bibliography

[1] BA Glass. *Annual Report*. 2021 (Cited on pages 1, 2).

[2] Kyeongjun Seo, Thomas F. Edgar, and Michael Baldea. "Optimal demand response operation of electric boosting glass furnaces". In: *Applied Energy* 269 (2020), p. 115077. ISSN: 0306-2619. DOI: doi.org/10.1016/j.apenergy.2020.115077 (Cited on page 4).

[3] Joan L. Pellegrino. "Glass Industry of the Future: Energy and Environmental Profile of the U. S. Glass Industry". In: (Apr. 2002). Report documenting the partnership between DOEs Office of Industrial Technologies and the U.S. glass industry. (Cited on page 4).

[4] Edgar D. Zanotto and John C. Mauro. "Two Centuries of Glass Research: Historical Trends, Current Status, and Grand Challenges for the Future". In: *International Journal of Applied Glass Science* 5.3 (2014), pp. 313–327. DOI: doi.org/10.1111/ijag.12087 (Cited on page 4).

[5] Edgar D. Zanotto and John C. Mauro. "The glassy state of matter: Its definition and ultimate fate". In: *Journal of Non-Crystalline Solids* 471 (2017), pp. 490–495. ISSN: 0022-3093. DOI: doi.org/10.1016/j.jnoncrysol.2017.05.019 (Cited on page 4).

[6] Alessandra Cantini et al. "Technological Energy Efficiency Improvements in Glass-Production Industries and Their Future Perspectives in Italy". In: *Processes* 10.12 (2022). ISSN: 2227-9717. DOI: 10.3390/pr10122653 (Cited on page 4).

[7] *GlassGlobal Group, Facts and Figures*. www.plants.glassglobal.com/. Accessed: 24-04-2023 (Cited on page 4).

[8] The European Container Glass Federation. *Glass Packaging Industry*. www.feve.org/glass-industry/. Accessed: 23-05-2023 (Cited on page 4).

[9] Thomas Parker. *Top five glass packaging manufacturers in the world by revenue*. www.nspackaging.com/news/glass-packaging-manufacturers/. Accessed: 23-05-2023. 2020 (Cited on page 4).

[10] James E. Shelby. *Introduction to Glass Science and Technology*. 2nd. Oxford University Press, 2005 (Cited on pages 5, 8).

[11] AIS Glass. *5 things you should know about flat glass*. www.aisglass.com/5-things-you-should-know-about-flat-glass/. Accessed: 13-06-2023. 2020 (Cited on page 5).

[12] Science Equip. *Common Lab Glassware and its Uses*. www.scienceequip.com.au/blogs/news/common-lab-glassware-and-its-uses. Accessed: 13-06-2023 (Cited on page 5).

[13] Roche Industry. *Common Lab Glassware and its Uses*. www.rocheindustry.com/glass-bottle-manufacturers-in-the-usa/. Accessed: 13-06-2023 (Cited on page 5).

[14] Mathieu Hubert. *Lecture 3: Basics of industrial glass melting furnaces*. IMI-NFG Course n Processing in Glass. 2015 (Cited on pages 5, 6).

[15] BA Academy Newcomers. *Glass Container Production Process*. Internal Training. 2022 (Cited on pages 6, 7, 10).

[16] Vishal Sardeshpande, U.N. Gaitonde, and Rangan Banerjee. "Model based energy benchmarking for glass furnace". In: *Energy Conversion and Management* 48.10 (2007), pp. 2718–2738. ISSN: 0196-8904. DOI: doi.org/10.1016/j.enconman.2007.04.013 (Cited on page 6).

[17] J. Cassiano, M.V. Heitor, and T.F. Silva. "Combustion tests on an industrial glass-melting furnace". In: *Fuel* 73.10 (1994), pp. 1638–1642. ISSN: 0016-2361. DOI: doi.org/10.1016/0016-2361(94)90144-9 (Cited on page 7).

[18] Paul A Bingham. "Design of New Energy-Friendly Compositions". In: *Fiberglass and Glass Technology: Energy-Friendly Compositions and Applications*. Ed. by Frederick T. Wallenberger and Paul A. Bingham. Springer, 2010. Chap. 7, pp. 267–351. DOI: 10.1007/978-1-4419-0736-3_7 (Cited on pages 8, 9, 17).

[19] Antonín Smrček. "Compositions of Industrial Glasses". In: *Fiberglass and Glass Technology: Energy-Friendly Compositions and Applications*. Ed. by Frederick T. Wallenberger and Paul A. Bingham. Springer, 2010. Chap. 6, pp. 229–266. DOI: 10.1007/978-1-4419-0736-3_6 (Cited on page 8).

[20] Richard Stormont. *Electrical melting and boosting for glass quality improvement*. 2010 (Cited on page 9).

[21] Jaroslav Staněk. "Theoretical and practical achievements in the electric melting of glass". In: *Journal of Non-Crystalline Solids* 80.1 (1986). International Symposium on Glass Proceedings of the Second Beijing Symposium on Glass, pp. 103–114. ISSN: 0022-3093. DOI: doi.org/10.1016/0022-3093(86)90383-2 (Cited on pages 9, 11, 20, 30, 31, 33, 41).

[22] Rudi Kessel. *Electrical boosting – a technology review*. 2007 (Cited on pages 9, 10).

[23] CelSian Tech Course. *Electrical Glass Melting (systems)*. 2022 (Cited on page 10).

[24] Krista Grayson. *Are Electric Furnaces the Future of Glass Manufacturing?* www.mo-sci.com/electric-furnaces-future-glass-manufacturing/. Accessed: 18-05-2023. 2019 (Cited on page 10).

[25] Richard L. Curran. "Mathematical Model of an Electric Glass Furnace: Effects of Glass Color and Resistivity". In: *IEEE Transactions on Industry Applications* IA-9.3 (1973), pp. 348–357. DOI: 10.1109/TIA.1973.349916 (Cited on pages 10, 31, 36, 41).

[26] Merve Durubal and Burçin Gül. "A Numerical Investigation of the Effect of Electric Boosting in an Oxy Fuel Fired Glass Fiber Furnace". In: 2017. URL: https://api.semanticscholar.org/CorpusID:218515674 (Cited on page 11).

[27] Luyao Li et al. "Three-Dimensional Glass Furnace Model of Combustion Space and Glass Tank with Electric Boosting". In: *Material Transactions* 60.6 (2019), pp. 1034–1043. DOI: 10.2320/matertrans.M2019044 (Cited on page 11).

[28] Juraj Raič et al. "CFD simulation aided glass quality and energy efficiency analysis of an oxy-fuel glass melting furnace with electric boosting". In: *Energy Conversion and Management: X* 15 (2022), p. 100252. ISSN: 2590-1745. DOI: https://doi.org/10.1016/j.ecmx.2022.100252 (Cited on page 11).

[29] Jaroslav Staněk. "Problems in electric melting of glass". In: *Journal of Non-Crystalline Solids* 123.1 (1990). XVth International Congress on Glass, pp. 400–414. ISSN: 0022-3093. DOI: doi.org/10.1016/0022-3093(90)90812-Z (Cited on pages 11, 14, 31, 41).

[30] Norman R. Gruenberg. "Effects of Electrical Connections and Phasing in Electrical Glass Melting Systems". In: *IEEE Transactions on Industry Applications* IA-8.1 (1972), pp. 76–81. DOI: 10.1109/TIA.1972.349740 (Cited on pages 11, 22–24, 31, 34, 36, 41).

[31] Jackson S. Stroud. "Molybdenum Electrodes in Glass Tanks". In: *IEEE Transactions on Industry Applications* IA-13.6 (1977), pp. 618–625. DOI: 10.1109/TIA.1977.4503467 (Cited on page 11).

[32] National Element. *Molybdenum Technical Data*. 2017 (Cited on page 16).

[33] Michael B. Heaney. "Electrical Measurement, Signal Processing, and Displays". In: ed. by John G. Webster. CRC Press, 2003. Chap. Electrical Conductivity and Resistivity, pp. 7–1. ISBN: 0-20-300940-1 (Cited on page 17).

[34] John Vienna. "Compositional Models of Glass/Melt Properties and their Use for Glass Formulation". In: *Procedia Materials Science* 7 (Dec. 2014). DOI: 10.1016/j.mspro.2014.10.020 (Cited on page 17).

[35] Alexander Flugel, David A. Earl, and Arun K. Varshneya. "Electrical resistivity of silicate glass melts calculation based on the SciGlass database". In: *New York State College of Ceramics* (2007) (Cited on pages 17, 48).

[36] Oleg V. Mazurin and Oleg A. Prokhorenko. “Electrical conductivity of glass melts”. In: *Properties of Glass-Forming Melts*. Ed. by David Pye, Innocent Joseph, and Angelo Montenero. 1st. Taylor & Francis, 2005. Chap. 10, pp. 295–337 (Cited on pages 17, 18, 47).

[37] A. K. Varshneya et al. “Modeling of glass making processes for improved efficiency: high temperature glass melt property database for modeling”. In: *Advances in Fusion and Processing of Glass III*. Ed. by Thomas P. Seward III, James R. Varner, and Helmut A. Schaeffer. 7th International Conference on Advances in Fusion and Processing of Glass. The American Ceramic Society, 2004, pp. 153–159 (Cited on pages 17, 28).

[38] Alexander Fluegel. Glass Properties. *Electrical resistivity calculator*. ww.glassproperties.com/resistivity. Germany. Accessed: 03-05-2023. 2007 (Cited on page 19).

[39] Alexander Fluegel. “Glass Viscosity Calculation Based on a Global Statistical Modeling Approach”. In: *Glass Technology - European Journal of Glass Science and Technology Part A* 48 (Feb. 2007), pp. 13–30 (Cited on page 20).

[40] Jaroslav Staněk and Jiří Matěj. “Electric melting of glass”. In: *Journal of Non-Crystalline Solids* 84.1 (1986). The physics and chemistry of glass and glass making, pp. 353–362. ISSN: 0022-3093. DOI: doi.org/10.1016/0022-3093(86)90797-0 (Cited on pages 20, 31, 40, 41).

[41] V. S. Golovin and V. G. Zheltov. “Determining Electrical Resistance Between Two Electrode Rods”. In: *Plenum Publishing Corporation* (1978), pp. 489–491 (Cited on page 20).

[42] Yunus A. Çengel. *Heat Transfer: A Practical Approach*. Ed. by McGraw-Hill. 2nd. 2002. ISBN: 0-20-300940-1 (Cited on page 25).

[43] Arthur Eugene Fitzgerald. *Electric machinery*. 4th ed. New York: McGraw-Hill, 1983. ISBN: 0070211450 (Cited on page 30).

Appendix A

Model Coefficients

Table A.1: Compositional coefficients for Mazurin electrical resistivity model, adapted [36]

Variables	**Coefficients**		
	600 °C	900 °C	1300 °C
Intercept	5.090	3.984	2.984
Al_2O_3	$3.340 \cdot 10^{-2}$	$3.120 \cdot 10^{-2}$	$2.890 \cdot 10^{-2}$
$(Al_2O_3)^2$	$-2.340 \cdot 10^{-3}$	$-1.350 \cdot 10^{-3}$	$-3.070 \cdot 10^{-4}$
K_2O	$2.120 \cdot 10^{-1}$	$1.686 \cdot 10^{-1}$	$6.850 \cdot 10^{-2}$
$(K_2O)^2$	$-1.040 \cdot 10^{-2}$	$-1.260 \cdot 10^{-2}$	$-1.770 \cdot 10^{-3}$
MgO	$-2.110 \cdot 10^{-2}$	$-2.750 \cdot 10^{-4}$	$4.390 \cdot 10^{-3}$
$(MgO)^2$	$-1.790 \cdot 10^{-3}$	$-3.800 \cdot 10^{-3}$	$-2.260 \cdot 10^{-3}$
$R'O$	$1.540 \cdot 10^{-1}$	$5.780 \cdot 10^{-2}$	$2.550 \cdot 10^{-2}$
$(R'O)^2$	$-1.940 \cdot 10^{-3}$	$-1.890 \cdot 10^{-3}$	$-3.000 \cdot 10^{-3}$
R_2O	$3.130 \cdot 10^{-1}$	$-2.850 \cdot 10^{-1}$	$-2.260 \cdot 10^{-1}$
$(R_2O)^2$	$7.760 \cdot 10^{-3}$	$6.460 \cdot 10^{-3}$	$4.290 \cdot 10^{-3}$
$R_2O * R'O$	$-4.780 \cdot 10^{-3}$	$-1.440 \cdot 10^{-3}$	$5.350 \cdot 10^{-4}$

Table A.2: Compositional coefficients for Fluegel electrical resistivity model, adapted [35]

Variables	**Coefficients**		
	1000 °C	1200 °C	1400 °C
Intercept	2.842	2.415	1.795
B_2O_3	$8.370 \cdot 10^{-3}$	0	0
Al_2O_3	$7.117 \cdot 10^{-2}$	$4.730 \cdot 10^{-2}$	$1.838 \cdot 10^{-2}$
Li_2O	$-9.614 \cdot 10^{-2}$	$-9.017 \cdot 10^{-2}$	$-7.401 \cdot 10^{-2}$
Na_2O	$-1.839 \cdot 10^{-1}$	$-1.625 \cdot 10^{-1}$	$-1.101 \cdot 10^{-1}$
$(Na_2O)^2$	$4.844 \cdot 10^{-3}$	$3.874 \cdot 10^{-3}$	$1.807 \cdot 10^{-3}$
$(Na_2O)^3$	$-5.240 \cdot 10^{-5}$	$-3.740 \cdot 10^{-5}$	$-1.040 \cdot 10^{-5}$
K_2O	$-1.453 \cdot 10^{-1}$	$-1.209 \cdot 10^{-1}$	$-5.532 \cdot 10^{-2}$
$(K_2O)^2$	$2.760 \cdot 10^{-3}$	$1.593 \cdot 10^{-3}$	$-1.657 \cdot 10^{-3}$
$(K_2O)^3$	$-2.120 \cdot 10^{-5}$	$-2.200 \cdot 10^{-6}$	$4.990 \cdot 10^{-5}$
MgO	$1.529 \cdot 10^{-2}$	$5.160 \cdot 10^{-3}$	0
CaO	$2.759 \cdot 10^{-2}$	0	$-6.140 \cdot 10^{-3}$
$(CaO)^2$	0	$-3.800 \cdot 10^{-4}$	$-5.030 \cdot 10^{-4}$
SrO	$1.648 \cdot 10^{-2}$	$5.190 \cdot 10^{-3}$	$-3.600 \cdot 10^{-3}$
BaO	$3.265 \cdot 10^{-2}$	0	$-8.540 \cdot 10^{-3}$
ZrO_2	$1.101 \cdot 10^{-1}$	$3.420 \cdot 10^{-2}$	0
ZnO	$-9.740 \cdot 10^{-3}$	$-1.436 \cdot 10^{-2}$	$-1.499 \cdot 10^{-2}$
PbO	$1.396 \cdot 10^{-2}$	0	$-9.700 \cdot 10^{-3}$
$B_2O_3 * Al_2O_3$	$-6.400 \cdot 10^{-3}$	$-4.637 \cdot 10^{-3}$	$-2.288 \cdot 10^{-3}$
$B_2O_3 * K_2O$	$9.835 \cdot 10^{-3}$	$5.114 \cdot 10^{-3}$	$1.709 \cdot 10^{-3}$
$B_2O_3 * MgO$	$1.413 \cdot 10^{-3}$	$1.891 \cdot 10^{-3}$	$1.399 \cdot 10^{-3}$
$Al_2O_3 * Li_2O$	$-6.459 \cdot 10^{-3}$	$-2.965 \cdot 10^{-3}$	0
$Al_2O_3 * Na_2O$	$-3.263 \cdot 10^{-3}$	$-1.979 \cdot 10^{-3}$	$-6.310 \cdot 10^{-4}$
$Al_2O_3 * K_2O$	$-1.344 \cdot 10^{-3}$	$-6.270 \cdot 10^{-4}$	0
$Li_2O * Na_2O$	$3.791 \cdot 10^{-3}$	$3.385 \cdot 10^{-3}$	$2.441 \cdot 10^{-3}$
$Li_2O * K_2O$	$6.357 \cdot 10^{-3}$	$5.200 \cdot 10^{-3}$	$3.822 \cdot 10^{-3}$
$Li_2O * CaO$	$-4.558 \cdot 10^{-3}$	$-3.209 \cdot 10^{-3}$	$-2.514 \cdot 10^{-3}$
$Na_2O * K_2O$	$7.281 \cdot 10^{-3}$	$5.861 \cdot 10^{-3}$	$2.823 \cdot 10^{-3}$
$Na_2O * MgO$	$-1.447 \cdot 10^{-3}$	$-9.750 \cdot 10^{-4}$	$-5.840 \cdot 10^{-4}$
$Na_2O * CaO$	$-9.940 \cdot 10^{-4}$	$5.100 \cdot 10^{-4}$	$7.540 \cdot 10^{-4}$
$K_2O * CaO$	$2.880 \cdot 10^{-4}$	$1.641 \cdot 10^{-3}$	$1.607 \cdot 10^{-3}$
$Na_2O * K_2O * CaO$	$3.320 \cdot 10^{-4}$	$1.610 \cdot 10^{-4}$	0

Appendix B

Dimensional Parameters

Table B.1: Distance between each pair of electrode

Terminals Connected	Pair	Distance (m)
Terminals R1-R2	E1-E9	10.255
	E1-E10	9.710
	E2-E9	10.983
	E2-E10	10.476
Terminals R1-S1	E1-E7	7.391
	E1-E8	7.334
	E2-E7	7.334
	E2-E8	7.391
Terminals R1-S2	E1-E11	8.213
	E1-E12	8.058
	E2-E11	9.106
	E2-E12	8.967
Terminals R1-T1	E1-E3	2.286
	E1-E4	3.200
	E2-E3	1.372
	E2-E4	2.286
Terminals R1-T2	E1-E6	7.682
	E1-E5	8.002
	E2-E6	7.461
	E2-E5	7.682
Terminals R2-S1	E9-E7	8.967
	E9-E8	8.058
	E10-E7	9.106
	E10-E8	8.213
Terminals R2-S2	E10-E12	4.572
	E9-E12	5.486
	E10-E11	3.658
	E9-E11	4.572

Table B.2: Distance between each pair of electrode (cont.)

Terminalss Connected	Pair	Distance (m)
Terminals R2-T1	E9-E3	12.124
	E9-E4	12.909
	E10-E3	11.667
	E10-E4	12.480
Terminals R2-T2	E9-E5	11.243
	E9-E6	10.332
	E10-E5	11.355
	E10-E6	10.454
Terminals S1-S2	E8-E11	9.710
	E8-E12	10.255
	E7-E11	10.476
	E7-E12	10.983
Terminals S1-T1	E8-E3	7.682
	E8-E4	8.002
	E7-E3	7.461
	E7-E4	7.682
Terminals S1-T2	E8-E6	2.286
	E8-E5	3.200
	E7-E6	1.372
	E7-E5	2.286
Terminals S2-T1	E11-E3	10.454
	E11-E4	11.355
	E12-E3	10.332
	E12-E4	11.243
Terminals S2-T2	E11-E5	12.480
	E11-E6	11.667
	E12-E5	12.909
	E12-E6	12.124
Terminals T1-T2	E3-E5	7.391
	E3-E6	7.334
	E4-E5	7.334
	E4-E6	7.391

Appendix C

Results Values

Table C.1: Effective power dissipated from each electrode pair

Terminals	Pairs	R_{ik} (Ω)	$P_{u,\ ik}$ (kW)			
			Scenario 1	**Scenario 2**	**Scenario 3**	**Scenario 4**
R1-R2	E1-E9	0.0930	7.84	5.21	7.27	3.11
	E1-E10	0.0921	7.92	5.26	7.34	3.14
	E2-E9	0.0940	7.75	5.15	7.19	3.07
	E2-E10	0.0933	7.81	5.19	7.25	3.10
R1-S1	E1-E7	0.0877	0.103	0.0114	0.285	0
	E1-E8	0.0876	0.103	0.0114	0.286	0
	E2-E7	0.0876	0.103	0.0114	0.286	0
	E2-E8	0.0877	0.103	0.0114	0.285	0
R1-S2	E1-E11	0.0894	0.0448	0.0112	0.0112	0.280
	E1-E12	0.0891	0.0449	0.0112	0.0112	0.281
	E2-E11	0.0910	0.0439	0.0101	0.0101	0.275
	E2-E12	0.0908	0.0440	0.0110	0.0110	0.275
R1-T1	E1-E3	0.0690	0.710	2.45	0.232	0.522
	E1-E4	0.0746	0.657	2.28	0.215	0.485
	E2-E3	0.0608	0.806	2.78	0.264	0.593
	E2-E4	0.0692	0.708	2.45	0.232	0.522
R1-T2	E1-E6	0.0883	36.8	40.8	33.0	43.5
	E1-E5	0.0890	36.5	40.5	32.8	43.2
	E2-E6	0.0879	37.0	41.0	33.2	43.8
	E2-E5	0.0884	36.8	40.8	33.0	43.5
R2-S1	E9-E7	0.0908	6.34	4.86	4.86	3.18
	E9-E8	0.0891	6.47	4.95	4.95	3.24
	E10-E7	0.0910	6.33	4.84	4.84	3.17
	E10-E8	0.0894	6.44	4.93	4.93	3.23

Table C.2: Effective power dissipated from each electrode pair (cont.)

Terminals	**Pairs**	R_{ik} (Ω)	$P_{u,\,ik}$ (kW)			
			Scenario 1	**Scenario 2**	**Scenario 3**	**Scenario 4**
R2-S2	E10-E12	0.0800	7.81	6.61	7.81	6.05
	E9-E12	0.0829	7.54	6.38	7.54	5.84
	E10-E11	0.0764	8.18	6.92	8.18	6.33
	E9-E11	0.0800	7.81	6.61	7.81	6.05
R2-T1	E9-E3	0.0956	12.1	12.8	9.41	5.53
	E9-E4	0.0966	12.0	12.7	9.31	5.47
	E10-E3	0.0950	12.2	12.9	9.47	5.57
	E10-E4	0.0961	12.0	12.8	9.37	5.50
R2-T2	E9-E5	0.0944	74.7	71.2	67.8	66.1
	E9-E6	0.0931	75.8	72.2	68.8	67.1
	E10-E5	0.0946	74.6	71.1	67.7	66.0
	E10-E6	0.0933	75.7	72.1	68.6	66.3
S1-S2	E8-E11	0.0921	0.0109	0.0434	0.174	0.272
	E8-E12	0.0930	0.0108	0.0430	0.172	0.269
	E7-E11	0.0933	0.0107	0.0429	0.172	0.268
	E7-E12	0.0940	0.0106	0.0425	0.170	0.266
S1-T1	E8-E3	0.0883	1.13	2.22	0.917	0.408
	E8-E4	0.0890	1.12	2.20	0.910	0.405
	E7-E3	0.0879	1.14	2.23	0.922	0.410
	E7-E4	0.0884	1.13	2.22	0.917	0.408
S1-T2	E8-E6	0.0690	52.2	52.2	50.5	55.8
	E8-E5	0.0746	48.3	48.5	46.9	51.7
	E7-E6	0.0608	59.2	59.3	57.3	63.3
	E7-E5	0.0692	52.0	52.2	50.5	55.8
S2-T1	E11-E3	0.0933	0.868	1.54	0.268	0.0107
	E11-E4	0.0946	0.856	1.52	0.264	0.0106
	E12-E3	0.0931	0.870	1.55	0.269	0.0107
	E12-E4	0.0944	0.858	1.52	0.265	0.0106
S2-T2	E11-E5	0.0961	36.2	36.2	31.5	33.8
	E11-E6	0.0950	36.6	36.6	31.8	34.2
	E12-E5	0.0966	36.0	36.0	31.3	33.6
	E12-E6	0.0956	36.4	36.4	31.6	34.0
T1-T2	E3-E5	0.0877	28.5	25.2	28.5	35.8
	E3-E6	0.0876	28.6	25.2	28.6	35.8
	E4-E5	0.0876	28.6	25.2	28.6	35.8
	E4-E6	0.0877	28.5	25.2	28.5	35.8